<u>Title:</u> Annexin- and calcium-regulated priming of legume root cells for endosymbiotic infection

Authors:

Ambre Guillory[1§], Joëlle Fournier[1§], Audrey Kelner[1§], Karen Hobecker[2], Marie-Christine Auriac[1], Lisa Frances[1], Anaïs Delers[1], Léa Pedinotti[4], Aurélie Le Ru[3], Jean Keller[4], Pierre-Marc Delaux[4], Caroline Gutjahr[2], Nicolas Frei Dit Frey[4] and Fernanda de Carvalho-Niebel[1*]

Affiliations :

[1]LIPME, INRAE, CNRS, Université de Toulouse, Castanet-Tolosan, France.

[2]Max-Planck-Institute of Molecular Plant Physiology, Potsdam-Golm, Germany.

[3]FRAIB-TRI imaging platform, Université de Toulouse, CNRS, UPS, Castanet-Tolosan, France.

[4]LRSV, Université de Toulouse, CNRS, UPS, Toulouse INP, Castanet-Tolosan, France.

[§]these authors contributed equally to this work

[*]Correspondence to: Fernanda de Carvalho-Niebel (fernanda.de-carvalho-niebel@inrae.fr)

Abstract

Legumes establish endosymbioses with arbuscular mycorrhizal (AM) fungi or rhizobia bacteria to improve mineral nutrition. Symbionts are hosted in privileged habitats, root cortex (for AM fungi) or nodules (for rhizobia) for efficient nutrient exchange. To reach these habitats, plants form cytoplasmic bridges, which are key to predicting and guiding the cellular route of entry of fungal hyphae or rhizobia-filled infection threads (ITs). However, the underlying mechanisms are poorly studied. Here we show that unique ultrastructural changes and Ca^{2+} spiking signatures, closely linked to MtAnn1 annexin accumulation, accompany rhizobia-associated bridge formation. Loss of *MtAnn1* function in *M. truncatula* affects Ca^{2+} spike amplitude, cytoplasmic configuration and rhizobia infection efficiency, consistent with a role of MtAnn1 in regulating infection priming. *MtAnn1,* which evolved in species establishing intracellular symbioses, is also AM-symbiosis-induced and required for proper arbuscule formation. Together, we propose that MtAnn1 is part of an ancient Ca^{2+}-regulatory module for transcellular endosymbiotic infection.

Introduction

Plants benefit from associations with microbes in the soil which improve the acquisition of essential nutrients for growth. These associations include the ancestral symbiosis with arbuscular mycorrhizal (AM) fungi providing phosphorous, or the more recently evolved interactions with endosymbiotic bacteria for nitrogen acquisition[1-3]. Microbial endosymbionts are hosted in privileged intracellular niches, where optimal conditions are met for efficient nutrient exchange (e.g. the root cortex hosting arbuscules formed by AM fungi, or root nodules, hosting nitrogen-fixing bacteria). Extensive studies on model legumes such as *Medicago truncatula*, combined with evolution-based studies across a broad species range revealed that nodule-forming nitrogen-fixing endosymbiosis (RNS) evolved ~100 million years ago in species from related angiosperm plant lineages, by co-opting signalling components from the ancient AM symbiosis and recruiting new key genes through neo-functionalization and/or rewiring of expression[2,4,5]. These endosymbioses share a common symbiotic pathway that uses calcium (Ca^{2+}) as a key secondary messenger to trigger downstream signalling[3,6]. Upon perception of mycorrhizal Myc and rhizobial Nod factor signals, Ca^{2+} oscillations (spiking) are triggered in and around the root hair nucleus through the concerted action of nuclear envelope channel/pump complexes[3,6,7]. While Ca^{2+} spiking is critical in the nucleus (after its decoding by Ca^{2+}/calmodulin-dependent protein kinases CCaMK or Does not Make Infection, DMI3)[8,9] to regulate host transcriptional reprogramming[10-12], the functional relevance of sustained Ca^{2+} spiking in the cytoplasmic compartment has not yet been established. The rhizobia- and AM-induced *MtAnn1*[13] and *MtAnn2*[14] genes, which encode cytosolic Ca^{2+}-binding annexins that can bind to membranes to modulate a variety of Ca^{2+} -regulated processes (e.g. ion conductance, exocytosis/endocytosis)[15,16], are potential players in this process.

Following signal exchange to reach compatibility, infection of root tissues by AM fungi or rhizobia bacteria occurs in most legumes transcellularly, through the *de novo* construction of apoplastic compartments, delimited by host cell wall/ membrane interfaces, which physically separate microsymbionts from the host cytoplasm[17-19]. The hyphae of AM fungi progress through epidermal and cortical root tissues until the fungus reaches the inner cortex to form

65 highly branched arbuscules inside plant cells. Arbuscules comprise a massive network of
66 membrane tubules at the symbiotic host-fungus interface[20,21], which likely ensures the release
67 of nutrients, particularly phosphate, to the plant. In RNS, rhizobia enter the roots of most
68 legume species *via* apoplastic tubular structures called infection threads (ITs)[18,19] that grow
69 from root hairs to the developing nodule underneath[22] under the influence of key plant
70 hormones, intercellular signalling and long-distance regulatory pathways[23-25].

71 ITs are formed in root hairs after rhizobia are entrapped and enclosed in a globular infection
72 chamber[26]. This plant-driven process requires targeted cell wall remodelling at the IT
73 interface[26,27] for polar growth, under the control of the infectosome protein complex[28-30].
74 Transcellular IT infection also imposes tight regulation of the plant's cell cycle status through
75 the recruitment of mitotic regulators in root hairs and acquisition of specific pre-mitotic states
76 before and during IT passage in the cortex[31-34]. Finally, the route of IT entry is also fine-tuned
77 by the host, which creates a broad cytoplasmic column filled with endoplasmic reticulum (ER)
78 and surrounded by microtubule arrays to guide IT progression[35,36]. In root hairs, this bridge
79 connects the tip of the IT to the nucleus to direct IT elongation. In the adjacent cortex,
80 differentiated root cells with a large central vacuole enter an activated state (hereafter termed
81 pre-infection priming), with characteristic transvacuolar cytoplasmic strands emanating from
82 the nucleus before a transvacuolar cytoplasmic bridge, the pre-infection thread (PIT[37]), forms
83 in anticipation of future IT passage. PIT bridges have been reported to occur in nodules of
84 several legume and actinorhizal species[37-39]. Moreover, PIT bridges closely resemble Pre-
85 Penetration Apparatus (PPA)[17,40] cytoplasmic columns that precede AM fungal hyphae
86 transcellular passage. The fact that PIT/PPA-like remodelling is not seen in pathogen
87 interactions[41], suggests their specific and probably ancient recruitment for endosymbiosis.
88 Parallels have been drawn between PIT/PPA and premitotic phragmosome transvacuolar
89 bridges formed in cells preparing for mitosis, as these processes share similarities in tightly
90 controlling plant cell division status, membrane trafficking and microtubule dynamics[33,34,38,42].

91 The development of fluorescent protein fusions labelling the endoplasmic reticulum
92 network (ER) has made it possible to visualize the dynamics of ER-enriched bridge remodelling
93 *in vivo* during PPA/PIT formation[35,40,43]. Complementary *in vivo* studies using Cameleon Ca^{2+}
94 sensors revealed that primed cortical cells exhibit a low-frequency Ca^{2+} spiking signature that
95 switches to high frequency at the onset of infection by AM fungi or rhizobia[43]. CCaMK/DMI3
96 is critical for PPA formation in *Medicago*[41]. Moreover, a gain-of-function variant in *Lotus* can
97 trigger cytoplasmic remodelling in the cortex in the absence of symbionts[44]. Thus,
98 CCaMK/DMI3-mediated signalling can bypass early symbiotic activation to trigger the priming
99 response in the cortex. These studies suggest that cytoplasmic bridge reprogramming involves
100 fine-tuning of Ca^{2+} spiking signatures, but the underlying genetic pathways or molecular
101 players have not been identified.

102 In this study, using resolutive microscopy methods in different *M. truncatula* genetic
103 backgrounds, we provide novel insights on ultrastructural rearrangements and *in vivo* Ca^{2+}
104 signalling dynamics in plant cells preparing for rhizobia infection. We show that an intimate
105 link between specific Ca^{2+} spiking signatures and the accumulation of annexin MtAnn1
106 characterises this priming response. MtAnn1 is a clear indicator of cytoplasmic reprograming
107 for infection, and its expression in this context is induced by the master symbiotic transcription
108 factor Nodule Inception (NIN)[4]. Through phylogenetics and mutant phenotyping, we provide
109 evidence that *MtAnn1*, recruited during evolution in plants establishing root endosymbioses,
110 likely plays an ancestral role for successful rhizobia and AM fungi infection. We propose that

111 *MtAnn1* was recruited to shape calcium-regulated transvacuolar cytoplasmic rearrangements
112 for efficient endosymbiotic infection.

113

114 **Results**

115 **Cell-specific ultrastructural changes in plant cells prior to IT entry**

116 PIT bridge formation is a widespread process in RNS nodules[37,39], but detailed studies of
117 this process are lacking. Previous work in *M. sativa* and *M. tuncatula skl* mutant roots showed
118 that microtubule rearrangements accompany PIT formation[38], however overall cellular
119 features underlying this process remain unknown. Here, we set up an adapted methodology
120 to gain access to ultrastructural changes underlying rhizobia pre-infection priming in *M.*
121 *truncatula* roots. Segments of early infected roots, harvested 5-6 dpi with rhizobia, were
122 prepared for light and transmission electron microscopy (TEM) using an Epon-embedding
123 procedure. These analyses revealed specific cytoplasmic rearrangements in primed outer
124 cortical cells (C1) next to an infected root hair site (Fig. 1A-C) compared to mock control (Fig.
125 1H-J) root samples. TEM analyses showed that the thick cytoplasmic bridge was highly
126 enriched in endoplasmic reticulum (ER) (white arrows, Fig. 1E) and large quantities of small
127 vacuole-like structures with sizes ranging from 0.5 to 5 µm (v in Fig. 1E). These activated cells
128 also featured significant and unusually high mitochondrial clustering around the nucleus (Fig.
129 1E and Fig. S1). This mitochondria-nuclei association was consistently observed in independent
130 pre-infection (PI) primed cells (Fig. 1E and Fig. S1B-G) compared to actively dividing cells in the
131 nodule primordia (NP) (Fig. 1D, Fig. S1B-C and S1H-K). At a later stage, when the IT had
132 progressed across this small vacuole- and ER-rich cytoplasmic bridge, the nucleus was often
133 found in close proximity to the IT (Fig. 1F-G). Thus, the plant nucleus not only guides the
134 progression of ITs but also establishes close physical interactions with them. Overall, drastic
135 ultrastructural changes take place specifically in outer cortical cells (C1 or C2) primed for
136 rhizobia infection, namely a unique transcellular cytoplasmic organization, enriched with ER,
137 small vacuole-like structures and a significant increase in mitochondria-nucleus association.

138

139 **MtAnn1 and Ca^{2+} spiking dynamics mark symbiotically engaged and infected plant cells**

140 Ca^{2+} spiking responses are transiently regulated in cortical cells preparing for infection[43], but
141 how these responses relate to cytoplasmic remodelling is unknown. To study this, we used an
142 *in vivo* approach based on co-imaging a fluorescent Ca^{2+}sensor and a cytoplasmic marker to
143 simultaneously monitor Ca^{2+} spiking and cytoplasmic remodelling in individual cells. We used
144 *M. truncatula* A17 (wild-type) and the supernodulating mutant *sunn*, which shows wild-type
145 infection but at higher levels, facilitating live imaging studies of early rhizobia infection
146 events[26,28,45]. These *in vivo* analyses cannot provide as much data from the wild-type
147 background in which infection thread events are more rare than in *sunn*. However, results
148 were confirmed in the two genetic backgrounds (*A17*, *sunn*) by independent experiments.
149 Furthermore, as sites of interest were individually imaged multiple times in living roots,
150 responses were dynamically monitored and confirmed overtime by follow-up observations.

151 We used the red fluorescent nuclear NR-GECO1 sensor for Ca^{2+}imaging because of its
152 better compatibility with the green fluorescence cytoplasmic marker and higher sensitivity to
153 detect symbiotic Ca^{2+} spiking, as compared to a Förster resonance energy transfer (FRET)
154 cameleon sensor[46]. To validate this sensor in our system, we first monitored Ca^{2+} spiking in *S.*

155 *meliloti*-responsive root hairs of the nodulation susceptible zone, just below the infection
156 zone, in both *A17* and *sunn,* 1-4 dpi with rhizobia. Using NR-GECO1, we confirmed that *S.*
157 *meliloti* triggers periodic, high-frequency Ca^{2+} spiking in these root hairs with profiles
158 indistinguishable from those induced by purified Nod factors, as previously reported[46,47] (Fig.
159 S2 and Movies 1-2). Subsequent analysis of rhizobia-infected sites in *sunn* at 2-7 dpi, revealed
160 specific low frequency Ca^{2+} spiking profiles in the outer cortex underlying rhizobia infection
161 sites (Fig. S3). Cortical cells that spiked (Fig. S3B, D, F and H), included those that later became
162 infected (Fig. S3C and G). Furthermore, only cortical cells in close contact with the infected
163 epidermal cell spiked, while other distant cortical cells did not. This suggests that potential
164 short distance signalling from the infected cell is required for pre-infection priming of cortical
165 cells. Our results are consistent with previous data using a FRET-cameleon Ca^{2+} probe[43], and
166 confirm that low-frequency Ca^{2+} spiking is associated with rhizobial pre-infection priming of
167 cortical cells.

168 *MtAnn1*, encoding a cytosolic Ca^{2+} and membrane-binding annexin protein, is induced by
169 rhizobia both in root hairs and in outer cortical cells preparing for infection[13,31], where Ca^{2+}
170 spiking responses are coincidently transiently regulated (Fig. S3)[43]. Thus, the use of a cytosolic
171 MtAnn1-GFP fusion expressed under its native rhizobia-induced promoter seemed a suitable
172 tool to monitor cytoplasmic remodelling during rhizobia infection. Comparative localisation
173 analyses were performed in *M. truncatula* A17 and/or *sunn* genotypes using a GFP-ER marker,
174 which labels the cytoplasmic ER endomembrane network, and the MtAnn1-GFP fusion. This
175 revealed similar labelling of root hair cytoplasmic bridges by both markers (Fig S4). Co-
176 localization studies confirmed that MtAnn1-GFP and a red mcherry-ER fusion co-labelled
177 cytoplasmic bridges in both root hair (Fig. S5) and cortical cells (Fig. S6). MtAnn1-GFP fusion,
178 expressed under its native promoter, specifically labels cytoplasmic bridges of pre-infection
179 primed cells (Fig. S6A-B) and no labelling was observed in non-activated cells in the vicinity of
180 the red mCherry-ER marker (driven by the p35S) labelling the cytoplasm. Combined, these
181 data support the conclusion that the MtAnn1-GFP fusion specifically marks cytoplasmic
182 bridges, where it partially co-localizes with the ER network.

183 Co-expression of red NR-GECO1 Ca^{2+} sensor and green MtAnn1-GFP fusion was then used
184 to live track the spatio-temporal dynamics of Ca^{2+} spiking and MtAnn1 accumulation
185 simultaneously in *M. truncatula* A17. The MtAnn1/NR-GECO1 double-labelling greatly
186 facilitated detection of root hairs in early stages of bacterial entrapment (RHE) and IT polar
187 growth (IT). RHE- or IT- root hairs consistently showed both MtAnn1-GFP fusion signal and
188 high frequency Ca^{2+} spiking profiles (Fig. 2A-B, F). However, the amplitude of Ca^{2+} spikes
189 dropped significantly from RHE to IT stage root hairs (Fig. 2C-E). Conversely, relative levels of
190 MtAnn1-GFP fluorescence tended to increase in IT versus RHE root hairs (Fig. 2A-B and Fig.
191 S7), consistent with root hair transcriptome data[31]. Overall, our data suggest that decreased
192 Ca^{2+} spiking amplitude and increased MtAnn1 levels are associated with polar IT growth.

193 MtAnn1-GFP also labelled cytoplasmic bridges of cortical cells primed for infection in both
194 wild-type A17 and *sunn* (Fig. 3A-C, Fig. S6 and S8). MtAnn1-GFP-labelled cells were those in
195 close contact with the infected root hair, which consistently showed low frequency Ca^{2+}
196 spiking. Furthermore, this low-frequency Ca^{2+} spiking profile switches to a high-frequency
197 pattern when the cortical cell is infected (Fig. S8), consistent with previously published data[43].
198 Strikingly, nearby cortical cells not labelled with MtAnn1 did not show any spike in both A17
199 and *sunn* (Fig. 3 and Fig. S8). Collectively, our data establish that IT development and pre-

200 infection priming involve stage- and cell-type-specific Ca^{2+} spiking signatures closely linked to
201 MtAnn1-GFP bridge accumulation.

202

203 **Rhizobia root hair infection is required for pre-infection priming of adjacent cortical cells**

204 MtAnn1-GFP labelling and Ca^{2+} spiking mark primed outer cortical cells (Fig 3 and Fig S8),
205 but it is unclear if IT formation is required for this process. Co-expression of NR-GECO1 and
206 MtAnn1-GFP in infection-defective *ern1* (*ERF Required for Nodulation 1*)[48-50], revealed that
207 Ca^{2+} spiking and cytoplasmic-bridge formation are still seen in root hairs with arrested
208 chambers (Fig. S9A-C). MtAnn1-GFP labelling and Ca^{2+} spiking were also seen in the outer
209 cortex adjacent to root hairs with arrested-infections in *ern1* (Fig. S9D-F), but the pattern
210 appeared to be deregulated (more cells labelled with MtAnn1-GFP or Ca^{2+} spiking sometimes
211 in *MtAnn1* unlabelled cells, never seen in the wild-type control A17 or *sunn*, Fig. 3 and Fig. S8).
212 This suggests that ERN1 is not required to promote pre-infection priming, but in its absence
213 the priming response is deregulated.

214 CCaMK/DMI3 is critical for PPA formation in *Medicago*[41], however, it is unknown if it is also
215 required for PIT formation. Since *dmi3*[8] is impaired in root hair infection, it is not possible to
216 access PIT formation in this genetic background. We thus took advantage of stable transgenic
217 lines complemented with DMI3 only in root hairs[51], to investigate if Ca^{2+} spiking and MtAnn1-
218 GFP could still label cortical cells in this line compared to wildtype A17 control (Fig. 3).
219 Complemented *dmi3* pEXT-DMI3 lines showed Ca^{2+} spiking, rescued IT development and
220 MtAnn1 labelling in root hairs (Fig. S9G and Movie 3). However, no Ca^{2+} spiking or MtAnn1-
221 GFP labelling was seen in the cortex, compared to the control A17 or *sunn* (Fig. 3 and Fig. S8).
222 No cytoplasmic remodelling in the cortex of *dmi3* pEXT-DMI3 could be detected by further
223 analysis of a constitutively expressed GFP (Fig. S9I-J). Thus, MtAnn1-labelled cytoplasmic
224 bridges were clearly visible only in infected root hairs of *dmi3* pEXT-DMI3 and not in adjacent
225 cortical cells (no MtAnn1 labelling or GFP-labelled cytoplasm remodelling, Fig S9). This
226 suggests that PIT infection priming uses a DMI3-dependent pathway that must be active in the
227 cortex.

228 Taken together, these analyses indicate that root hair infection chamber formation is
229 sufficient in *ern1* to trigger MtAnn1-GFP-labelled bridge in the root hair itself and adjacent
230 cortex. The absence of cortical priming in *dmi3* is consistent with the conclusion that, like in
231 PPA, DMI3 is required for PIT reprogramming.

232

233 **NIN controls pre-infection priming and the associated expression of *MtAnn1***

234 The master symbiotic transcription factor Nodule INception (NIN) is genetically
235 downstream of DMI3 and its mutation abolishes rhizobia-induced *MtAnn1* expression[31,52]. To
236 test if NIN is required for *MtAnn1* expression, we compared the spatio-temporal expression
237 profile of a *pMtAnn1:GUS* fusion in *M. truncatula* A17 wild-type and *nin* roots. In control
238 conditions, the *pMtAnn1:GUS* fusion was active in root tips, lateral roots and some
239 endodermal cells (Fig. 4A). Upon *S. meliloti* inoculation, strong promoter activity was detected
240 at rhizobial infection sites, both in root hairs and outer cortex (Fig. 4B-C), and later in other
241 nodule primordium cortical cells[13] but not in *nin* (Fig. 4D). This confirms the NIN-dependent
242 control of *MtAnn1* expression. Conversely, epidermal expression of NIN (*pEXPA:NIN*[53])
243 resulted in *pMtAnn1:GUS* fusion activity in the absence of rhizobia in *nin* (Fig. 4E-F). This

244 indicates that NIN can bypass early symbiotic signalling to promote *pMtAnn1:GUS* activity.
245 Transactivation assays in *Nicotiana benthamiana* (Fig. 4G and Fig. S10) showed that NIN can
246 transcriptionally activate *pMtAnn1:GUS*. This activation was abolished when a NIN mutated
247 version was used (Fig. 4G and Fig. S10). These data show that the expression of *MtAnn1* in
248 rhizobia infection sites is under NIN dependence and suggests that NIN is a possible direct
249 MtAnn1 regulator.

250 *nin* fails to form infection chambers and ITs but can still trap rhizobia in a curled root hair[26].
251 The question remains if a cytoplasmic bridge can still form in *nin*. To assess this, we examined
252 cytoplasmic bridge formation in *nin* transformed with *pEXPA:NIN* or a *pEXPA:GUS* control (Fig.
253 4H-M). Since *MtAnn1* is transcriptionally dependent on NIN (Fig. 4A-G), we could not use the
254 *pMtAnn1:MtAnn1-GFP* fusion for these studies, but instead used a *pENOD11:GFP-ER* fusion
255 co-expressed with *pEXPA:NIN* or *pEXPA:GUS* (control) in *nin*. Green GFP-ER fluorescence
256 marked the perinuclear ER network and the tip of growing root hairs in control and NIN-
257 complemented samples (Fig. 4H-J). However, thick cytoplasmic bridges marked by GFP-ER
258 were only detected in NIN-complemented root hairs (Fig. 4I-J). No GFP-ER signal was observed
259 in the root cortex of either control or NIN-complemented roots (Fig. 4K-M). Moreover, the
260 constitutive Ds-Red marker was also unable to detect cytoplasmic remodelling in *nin* (Fig. 4K-
261 M), whereas this marker allowed visualization of remodelling in control *sunn* roots (as
262 illustrated in Fig. S11). This suggests that a functionally active NIN in the cortex is required to
263 trigger cytoplasmic remodelling.

264 Together, these data infer that NIN acts downstream of DMI3 to control *MtAnn1* gene
265 transcription (possibly directly) and pre-infection priming.

266

267 ***MtAnn1* mutation affects efficiency of rhizobial infection and nodule differentiation**

268 Since *MtAnn1* expression is closely linked to early stages of rhizobial entry, we investigated
269 the impact of its mutation on rhizobial infection by analysing *M. truncatula Tnt1* R108
270 insertion mutant lines (Fig. S12). Promoter (*ann1-1*) or exonic mutant lines (*ann1-2* and *ann1-*
271 *3*) showed reduced (*ann1-1*) or nearly abolished (*ann1-2* and *ann1-3*) *MtAnn1* expression
272 compared with R108 and R108S, a wild-type sibling from the same mutant population (Fig.
273 S12A-B). Rhizobia infection was assessed in *ann1-2* and *ann1-3,* where *MtAnn1* expression was
274 most reduced, by monitoring bacterial β-galactosidase reporter activity in root and nodule
275 tissues. ITs formed in root hairs and progressed into the cortex in mutant roots, but with lower
276 efficiency (Fig. 5A-B). This did not affect nodule numbers, but their infection levels and relative
277 *VPY* expression (Fig. 5C-P and Fig. S12-S13). At 4 dpi, there was a consistent decrease in the
278 number of fully colonized NPs in mutants (40-50 %, compared to 70-90 % in wild-type lines)
279 (Fig. 5C). These NPs were often infected by multiple ITs compared with controls (Fig. 5D-J),
280 suggesting an inefficient process. A mixture of well and poorly colonized nodules was still
281 observed in mutant root systems at 10 dpi (Fig. 6M-P). Although not statistically significant,
282 there was a trend towards higher *MtAnn2* expression in rhizobia-inoculated roots of *ann1-2*
283 and *ann1-3* mutants than in wild-type lines, suggesting a possible compensatory effect (Fig.
284 S12).

285 Consistent with the R108 *ann1* mutant analyses, RNAi *MtAnn1* knockdown in *M. truncatula*
286 A17 resulted in reduced NP/nodule infection at 5 dpi (Fig. 5Q-T). Infected nodules in RNAi roots
287 show the same multiple ITs above as in annexin mutants (compare RNAi Fig. 5T, V with control
288 Fig. S, U, W). RNAi roots also contain abnormal NPs with poor or no colonization, with several

289 associated root hair ITs (Figure 5X-Z). These are not seen in control NPs (Fig. W, arrowheads).
290 Additional nodule number reduction was seen in RNAi roots, possibly due to the double
291 knockdown of *MtAnn1* and *MtAnn2* (Fig. 5Q and Fig. S12). Overall, impaired *MtAnn1* function
292 in mutant and RNAi contexts affected rhizobial root and nodule infection, in R108 and A17 *M.*
293 *truncatula* backgrounds.

294 While *ann1* mutants showed no major changes in root architecture or nodule number,
295 striking variations in shape (less elongated overall) and colour (paler pink) were seen at 21 dpi
296 (Fig. 6A-C and Fig. S13), reminiscent of potential differentiation and/or nitrogen fixation
297 defects[54]. To better understand why *ann1* nodules were smaller and less elongated, we
298 analysed thin and ultrathin sections of wild-type and mutant nodules. As the two mutant
299 alleles led to similar nodulation defects and the wild-type sibling (R108S) behaved reliably as
300 R108 (see Fig. 5 and S12-S13), we chose to perform these delicate thin/ultrathin sections on
301 one representative of each genotype (R108S and *ann1-3*). Meristematic (I), infection (II),
302 amyloplast-rich interzone (IZ) and nitrogen fixation (III) zones were clearly distinguished in
303 R108S nodules (Fig. 6D-H, N and Fig. S14). However, *ann1-3* nodules showed variable zonation
304 patterns, either wild-type-like or with significantly abnormally large IZ regions, sometimes
305 accompanied by senescing cells (arrows) (Fig. 6I-M, O-P and Fig. S14). Despite this IZ defect
306 (Fig. 6P), *ann1-3* nodules formed bacteroids. However, they did not appear to complete their
307 differentiation in Zone III-like bacteroids and instead remained interzone-type bacteroids[55],
308 imbedded in a white vesicle-enriched region (black arrows) (Fig. 6R-X). As a result, *ann1-3*
309 mutant nodules had reduced nitrogen-fixing capacity (Fig. 5F), which ultimately led to reduced
310 plant growth (Fig. S4D). Taken together, these results indicate that *Mtann1* mutant nodules
311 are affected in their differentiation and nitrogen fixing abilities.

312

313 **MtAnn1-dependent modulation of Ca^{2+} spiking and ultrastructural organization of the**
314 **cytoplasmic bridge**

315 As Ca^{2+} spiking and MtAnn1 dynamics were closely linked in the peri-nuclear regions of
316 primed cells (Figs. 2-3), we assessed if *MtAnn1* mutation impacts symbiotic Ca^{2+} spiking.
317 Although more challenging than previous live analysis in the hyper infectious *sunn* context (Fig.
318 2), we succeeded in monitoring Ca^{2+} spiking responses at infection sites in both wild-type
319 R108S and *ann1-3* transgenic roots expressing the NR-GECO1 Ca^{2+} sensor. Similarly, as seen in
320 sunn (Fig. 2), a drop in Ca^{2+} spiking amplitude was observed in R108S in IT-containing RHs
321 compared with RHE root hairs (Fig. 7A). Conversely, this drop was not clearly observed in *ann1-*
322 *3* (Fig. 7B). Likewise, a global deregulated Ca^{2+} spiking amplitude pattern was observed in many
323 S. *meliloti*-responsive root hairs of *ann1-3* compared with wild-type R108S, while Ca^{2+} spiking
324 frequency was not significantly changed in any root hair categories (Fig. 7C and S15). Together,
325 these data indicate a global deregulation of Ca^{2+} spiking amplitude in *ann1-3*, suggestive of
326 the need of *MtAnn1* for modulating symbiotic Ca^{2+} spiking responses.

327 Ca^{2+} spiking and MtAnn1 dynamics accompany cytoplasmic bridge formation (Fig. 2-3), so
328 we wondered how the deregulated Ca^{2+} spiking response in *ann1-3* (Fig. 7) could impact
329 cytoplasmic bridge formation. *MtAnn1* is expressed during root infection (Fig. 4), but also in
330 the nodule pre-infection and infection zones[56]. Thus, the defective nodule differentiation
331 phenotype of *ann-1-3* could be related to a possible deregulated infection in the nodule. We
332 thus analysed the cytoplasmic composition of infected cells in R108S and *ann1-3* apical nodule
333 zones by TEM, which can reveal ultrastructural organelle features and distribution that

334 confocal imaging cannot. In wild-type R108S, ITs progressed through a small vacuole-like
335 enriched cytoplasmic bridge containing a dense ER network (Fig. 7D-E, H-I and H'-I'), as shown
336 similarly in A17 (Fig. 1). In *ann-1-3*, the small vacuole-like and ER-enriched cytoplasmic
337 environment around the IT was strongly attenuated (Fig. 7F-G, J-K, J'-K'). Thus, mutation in
338 *MtAnn1* resulted in a deregulated Ca^{2+} spiking response and a change in the ER and vesicle
339 composition of the cytoplasmic bridge.

340

341 **_MtAnn1_ is required for efficient mycorrhizal root colonization**

342 Recently developed genomic and transcriptomic databases from around 300 plant species
343 establishing different types of endosymbioses enabled to address key endosymbiosis-related
344 ancestral gene functions[57]. We have thus exploited these extensive resources to trace the
345 evolutionary history of *MtAnn1*. Previous studies of the monophyletic plant annexin group,
346 mainly composed of angiosperm sequences, suggested their emergence through duplications
347 from a common ancestor prior to the monocot/eudicot split[58]. Consistent with these data, we
348 found that the *MtAnn1* annexin cluster likely arose from sequential pre-Angiosperms, Eudicots
349 and Papilionoideae-specific duplications (Fig S8). *MtAnn1* belongs to one of the Papilionoideae
350 duplicated clades, which mainly includes species that establish intracellular endosymbioses
351 (Fig. S16), except for *Caryophyallae* and *Cephalotus* (status uncertain). *Ann1* orthologs were
352 also detected in Papilionoideae species that lost RNS but maintained AMS. This indicates that
353 the function of *Ann1* is not restricted to RNS but could expand to AMS. Strikingly, *Ann1* from
354 different species show consistent transcriptional activation during both root nodule and AM
355 symbioses[5], suggesting an ancestral role in root endosymbiotic infection. To determine if
356 *MtAnn1* indeed plays a role during AMS, we first investigated if *MtAnn1* promoter activity was
357 spatio-temporally regulated in *M. truncatula* roots colonized by the AM fungus
358 *Rhizophagus irregularis*. Strong activation of the *pMtAnn1:GUS* fusion was only observed in
359 root segments colonized by *R. irregularis* at 4 wpi, especially in cortical cells containing
360 arbuscules (Fig. 8A-D). *R. irregularis* colonization rates were then monitored in *ann1-3*
361 compared to R108S wild-type roots at 6 dpi.

362 While R108S roots had dense colonization by *R. irregularis*, with cortex cells fully filled with
363 arbuscules, mutant roots had a lower proportion of colonized root sectors and arbuscule
364 density (Fig. 8E-H and K-L). In addition, arbuscules formed in the mutant showed a slightly but
365 significant reduction in length and this was associated with a trend increase in the expression
366 of the arbuscule senescence-related marker *MYB1*[59] (Fig. 8F-J and M-N). These data highlight
367 the importance of *MtAnn1* for the efficient establishment of the ancient AM symbiosis.

368

369 **Discussion**

370 Rhizobia root infection occurs transcellularly in most legumes via apoplastic IT structures
371 that grow polarly to reach the developing nodule. Plant cells engaged in this process form
372 cytoplasmic bridges that precede and accompany the route for ITs to progress. This process,
373 analogous to PPA bridges formed during AM symbiosis, is likely governed by common
374 ancestral cellular mechanisms, though knowledge remains limited. Here we report cell-
375 specific Ca^{2+} responses and cytoplasmic ultrastructural rearrangements that prime *M.*

truncatula plant cells for rhizobia infection. We show that this priming state, under DMI3-NIN genetic control, is marked by an intimate cellular link between Ca^{2+} spiking and annexin MtAnn1 accumulation. Moreover, MtAnn1 is needed for modulation of Ca^{2+} spiking responses and creation of an infection-permissive, dense, ER- and small vacuole-rich cytoplasmic environment. Ultimately, *MtAnn1* is required for successful root nodule differentiation and efficient AM root colonization, implying an ancient recruitment of *MtAnn1* in endosymbiosis. Our work supports the need to fine-tune cell-specific Ca^{2+}-spiking responses by annexin Ca^{2+} binding proteins for the transcellular passage of endosymbionts.

Organelle dynamics shaping rhizobia pre-infection priming

Ultrastructure dissection of plant cells preparing for transcellular rhizobia infection revealed marked enrichment and distribution of organelles during this process (Fig. 1). This priming state is seen only in a few outer cortical cells in close contact with the infected root hair cell (Fig. 1, 3 and S8), highlighting the likely need for signals from the infected cell to promote it. A marked clustering of mitochondria around the nucleus is observed in primed cells (Fig. 1 and S1). This may reflect the energy-demanding nature of this process. However, dividing nodule primordia cells with presumably high metabolic activity show no such enrichment. Alternatively, perinuclear mitochondria may mark a specific regulated cell cycle status, likely to occur in these cells[33,34,60] or contribute to modulating cytosolic Ca^{2+} oscillations, as shown in other systems[61].

Consistent with previous findings[35], TEM analysis revealed that a dense ER-rich network occupy the transcellular cytoplasmic bridge in primed or rhizobia infected *M. truncatula* cells (Fig. 1 and 7). The bridge is also rich in small vacuole-like structures[62], but we cannot exclude that multivesicular bodies (MVBs), seen in the PPA bridge, are part of this organelle population. Future use of molecular markers[62] may help discriminate between them. Dynamic changes in plant vacuole size have been reported to occur in different cell types, and in early meristematic cells this is thought to increase cytosolic area for subsequent daughter cell formation events[62,63]. An analogous need for increased cytosolic area is possibly required for IT passage. The concomitant reduction of small vacuoles and ER (involved in vacuole biogenesis[64]) in *MtAnn1* mutants (Fig. 7) raises the question of their functional interconnection in this process.

Role of MtAnn1 in modulating cell- and stage-specific symbiotic Ca^{2+} responses

High frequency Ca^{2+} spiking, triggered by Nod factors in root hairs is key for early rhizobia recognition [3,6,46]. Here, we showed that a second Ca^{2+} spiking phase occurs in root hairs undergoing rhizobia infection and involves a decrease in Ca^{2+} peak amplitude as ITs extend into root hairs (Fig. 2). This drop was also reported in root outer cortical cells crossed by an IT[43], consistent with this switch being key for IT progression. Ca^{2+} amplitude regulation fine-tunes different biological processes ranging from gene expression, stomatal closure, gravitropic responses to synaptic plasticity in animals[65-67]. The deregulated Ca^{2+} amplitude profile and defective infection caused by *MtAnn1* mutation (Fig. 5 and 7) points to a functional link between MtAnn1 and regulation of Ca^{2+} spiking amplitude during rhizobia infection.

418 We determined that Ca^{2+} spiking and strong MtAnn1-GFP labelling are hallmarks of rhizobia
419 infection and pre-infection priming (Fig. 3 and S8) and rely on the cell-autonomous activity of
420 DMI3 and NIN (Fig. 4 and S9). Thus, spatially distinct Ca^{2+} spiking responses are first triggered
421 in non-infected root hairs independently of DMI3-NIN[68,69], before DMI3-NIN-dependent Ca^{2+}
422 spiking is induced in cells engaged for infection. Using the NR-GECO1 sensor, we observe a
423 unique low frequency Ca^{2+} spiking only in primed cells of the cortex in both A17 and *sunn*
424 backgrounds (Fig. 3 and S8), in agreement with previous findings using a FRET-cameleon
425 sensor[43]. Although root hairs show similar remodelling and MtAnn1 labelling, they never show
426 such low frequency Ca^{2+} spiking, a signature likely reflecting a commitment state to infection.

427 In *Medicago*, symbiotic Ca^{2+} spiking is generated in the nucleoplasm and perinuclear
428 cytoplasm by the concerted action of nuclear envelope ion channels (DMI1, CNGC15), a Ca^{2+}
429 pump (MCA8), and under negative feedback regulation by a nuclear calmodulin (CaM2)[6,70].
430 MtAnn1 is a cytosolic phospholipid- and Ca^{2+}-interacting protein of the annexin family[13],
431 viewed as dynamic regulators that associate with membranes when intracellular Ca^{2+} levels
432 change[15,16]. Annexin family members are involved in the regulation of ion transport,
433 modulation of cytoplasmic Ca^{2+} signals and ROS signalling in diverse abiotic or biotic
434 responses[71-75]. Although predominantly cytoplasmic, annexins can also topologically associate
435 with the ER[76,77] and modulate the activity of Ca^{2+}-release channels[78]. As MtAnn1 partially
436 localizes to the ER network in cytoplasmic bridges (Fig. S4-S6), it may exert such a regulatory
437 function. The radical change in the cytosolic distribution of the ER and small vacuoles by the
438 *MtAnn1* mutation (Fig. 7) also establishes a functional link between MtAnn1 and the creation
439 of this specific cytoplasmic environment. Ca^{2+} orchestrates membrane trafficking and fusion,
440 while vacuoles, emitters and receivers of Ca^{2+} signals, can be directly affected by altered
441 cytosolic Ca^{2+} levels[79,80]. Annexins are Ca^{2+} sensing proteins involved in endomembrane
442 trafficking in plants[81], either in conjunction with the membrane fusion machinery or by
443 regulating exocytosis. Thus, MtAnn1 may directly or indirectly impact Ca^{2+}-regulated vesicle
444 trafficking and/or vacuole morphology. However, the biological relevance of such a dense
445 cytoplasmic strand for IT passage remains to be determined.

446

447 **Evolutionary recruitment of *MtAnn1* for root endosymbioses**

448 In *Mtann1* mutants, root infection by rhizobia is reduced (Fig. 5) and this culminates in
449 mature nodules with reduced size, altered shape, abnormal zonation and reduced nitrogen
450 fixation ability. These phenotypes are reminiscent of the reduced infection levels and nodule
451 size observed after *PvAnn1* RNAi knock-down in common bean[82]. Such phenotypes probably
452 stem from the early deregulated Ca^{2+} spiking, impaired cytoplasmic configuration and
453 consequently defective infection caused by the *MtAnn1* mutation. Furthermore, as *MtAnn1* is
454 expressed in nodule pre-infection and infection zones[56], the defective nodule differentiation
455 phenotype is likely a consequence of maintained deregulated infection in the nodule. Finally,
456 the close paralogue *MtAnn2*[14] may act redundantly with *MtAnn1* in early root infection (Fig.
457 5) where they are both co-expressed[31], but it is unlikely to compensate for *MtAnn1* loss of
458 function in nodules as it has a distinct spatial expression profile.

459 We showed that the subclade containing *MtAnn1* emerged mainly in plant species
460 establishing intracellular symbioses. Induced expression of *MtAnn1* in rhizobia and AM
461 symbioses and its requirement for proper formation of nitrogen-fixing nodules and cortical
462 arbuscules (Figs. 5 and 8) suggest ancestral and shared roles for *MtAnn1* in endosymbiotic

463 infection. We propose that *MtAnn1* fine-tunes oscillatory Ca^{2+} responses to create an optimal
464 dense cytoplasmic environment for rhizobia IT and AM fungi hyphae to progress. As *MtAnn1*
465 is transcriptionally regulated by NIN, even in the absence of symbiotic signalling (Fig. 4), we
466 hypothesize that *MtAnn1* is a direct target of NIN and that its evolutionary recruitment for
467 RNS involved the acquisition of putative NIN *cis*-regulatory motifs, which are indeed present
468 in the *MtAnn1* promoter. Since NIN is a major regulator in RNS[83], the AM-associated
469 expression of *MtAnn1* is possibly under the control of another, so far unidentified regulator.

470 In conclusion, we showed that cell specific Ca^{2+} spiking signals shape rhizobia pre-infection
471 priming to prepare the optimal dense cytoplasmic environment for IT passage in *Medicago*,
472 and MtAnn1 emerges as a modulator of this process. MtAnn1, necessary for efficient rhizobia
473 and AM colonization, may have been recruited during evolution to integrate an ancestral Ca^{2+}-
474 regulatory module for guiding endosymbiotic infection. MtAnn1, with a conserved K/H/RGD
475 protein-interacting motif[15], may work in partnership with other players, and discovering them
476 could help identify other critical components in this process.

477

478 **Methods**

479 **Plant materials and microbial strains**

480 *M. truncatula* Jemalong A17 and R108 wild-type ecotypes, a regenerated transgenic line (referred
481 to as A2) expressing the *p35S-GFP-HDEL* construct[35] as well as *sunn (sunn-2* allele)[84], *dmi3* (*dmi3-*
482 *1* allele)[8], *nin* (*nin-1* allele)[69] and *ern1* (*bit1* allele) & *ern1 ern2* (*bit1 ern2-1* alleles)[48,50] mutants
483 were used in this work. The *dmi3* line carrying the *pEXT:DMI3* construct[51], hereafter called
484 *dmi3* + *pEXT:DMI3*, was kindly provided by C. Remblière (LIPME, Toulouse). The three R108
485 *Tnt1* mutants carrying insertions in *MtAnn1* were obtained from Oklahoma State University
486 and are designated *ann1-1* (NF0830), *ann1-2* (NF17737) and *ann1-3* (NF4963). These lines
487 were self-crossed and genotyped by PCR and sequencing at each generation using primers -
488 *344 pMtAnn1-Fw*, *Mtr14183-Rev*, -914 *pMtAnn1-Fw*, *LTR6-* and *LTR4-* (Supplementary Table
489 S1). Homozygous mutants and sibling wild-type lines (referred to as WT) were selected for
490 seed multiplication and phenotyping. R108S is a wild-type sibling derived from line NF4963.
491 Seeds were scarified and surface-sterilized prior to germination on inverted soft agar plates[45]
492 and used for *A. rhizogenes* transformation or nodulation experiments. *N. benthamiana* seeds
493 were germinated in potting soil in glass-covered trays before transfer to pots (7 cm x 7 cm x
494 6.5 cm) at 21°C in a growth chamber under a 16h photoperiod and 70 µE/m/s light intensity
495 for 3 weeks until bacterial infiltration. The strains *A. rhizogenes* ARquA1, *A. tumefaciens*
496 GV3103 & GV3101 and *S. meliloti* 2011 (*Sm*2011-lac), constitutively expressing a *hemA-lacZ*
497 fusion, have been previously described[45]. The *S. meliloti* 2011 strain *Sm*2011-cCFP,
498 constitutively expressing a cyan fluorescent protein was kindly provided by P. Smit,
499 Wageningen (The Netherlands). *R. irregularis* spores (DAOM197198) were purchased from
500 Agronutrition (Labège, France).

501

502 **DNA constructs**

503 *pMtAnn1:MtAnn1-GFP*[13], *pENOD11:GFP-ER*[35] and *p35S-GFP-ER*[85] in pBIN121and *p2x35S-mCherry-*
504 *ER* in pBIN20[86] were used to study live pre-infection priming responses in *M. truncatula*.
505 *p2x35S:NR-GECO1* in pCAMBIA-CR1ΔDs-Red[46] was used to monitor Ca^{2+} spiking in *M.*
506 *truncatula*. *pMtAnn1:GUS* in pLP100[13], *pEXPA:NIN* in pK7WG2-R, *p35S:3xHA-NIN* and

507 *p35S:3xHA-NIN* in PAM-PAT35S-3xHA-GTW[53], were used in transcription activation studies in
508 *M. truncatula* or *N. benthamiana*. *p35S:MtAnn1-GFP* and *p35S:GFP* in pBIN121[13], were used
509 in mutant complementation studies. The *pMtAnn1:RNAi-MtAnn1* and *pMtAnn1:GUS* (control)
510 constructs were generated here by Golden-Gate cloning into the pCambia-CR1 vector[46].
511 Briefly, DNA fragments corresponding to 2,2 kb of the genomic *MtAnn1* sequence upstream of the
512 ATG, 942 bp of the *MtAnn1* coding sequence in sense and antisense orientations, and the GUS coding
513 sequence, were generated by PCR amplification using the primer pairs *pMtAnn1-GG-A-Fw*/*pMtAnn1-*
514 *GG-B-Rev*, *MtAnn1-ATG-GG-B-Fw*/*MtAnn1-STOP-GG-C-Rev*, *MtAnn1 antisens-STOP-GG-X-Fw*/*MtAnn1*
515 *antisens-ATG-GG-D-Rev* and *GUS-GG-B-Fw*/*GUS-GG-D-Rev*, respectively (Supplementary Table S1).
516 DNA fragments were then cloned into a pBluescript SK vector and validated by DNA
517 sequencing prior to Golden Gate assembly. Golden-Gate reactions with plasmids comprising
518 (i) the *MtAnn1* promoter, *MtAnn1* coding sequences (sense and antisense) and a 1,3 kb intron
519 spacer[23] or (ii) the *MtAnn1* promoter and the *GUS* coding sequence, were used to generate
520 *MtAnn1* RNAi (*pMtAnn1:MtAnn1 sens-intron-MtAnn1 antisens*) or GUS control
521 (*pMtAnn1:GUS*) constructs in the binary pCambia-CR vector. All binary vectors used for *A.*
522 *rhizogenes* transformation of *M. truncatula* (pLP100, pCambia, pK7WG2-R, pBIN121) include
523 a kanamycin resistance cassette in the T-DNA region. pK7G2-R and pCambia-CR1 vectors also
524 include a Ds-Red cassette.

525

526 **Generation of *M. truncatula* transgenic material**

527 *A. rhizogenes*-mediated transformation of *M. truncatula* A17 (WT, *sunn-2*, *ern1*, *ern1 ern2* and
528 *dmi3*) or R108 (WT sibling and *ann1-3*) was performed as described[45]. Briefly, germinated
529 seedlings had their root tips removed with a scalpel and were placed on Fahraeus medium
530 plates (12 cm x 12 cm) supplemented with 0.5 mM NH4NO3 and 20 mg/L kanamycin, before
531 inoculation with a drop (~3 µL) of *A. rhizogenes* aqueous suspension (OD600nm 0.5). For co-
532 transformation experiments with strains *pMtAnn1:MtAnn1-GFP* + *p2x35S:NR-GECO1*,
533 *p2x35S:NR-GECO1* + *pENOD11:GFP-ER*, *pEXPA:NIN* + *pENOD11:GFP-ER* or *pEXPA:NIN* +
534 *pMtAnn1:GUS* (in pLP100), equal volumes of bacterial suspensions were mixed prior to
535 seedling inoculation. The lower ¾ part of the plates were sealed with parafilm and placed
536 vertically in plastic boxes under controlled 16h light/ 8h dark photoperiod conditions, first at
537 20°C for 1 week, then at 25°C for two to three weeks. Composite *M. truncatula* plants with
538 kanamycin resistant roots were selected. In some experiments, kanamycin-resistant
539 composite roots were re-selected on the basis of constitutive fluorescence of the Ds-Red
540 marker (for pK7WG2-R *pEXPA:NIN* and pCAMBIA-CR1 *pMtAnn1:RNAi-MtAnn1* and
541 *pMtAnn1:GUS* constructs), fusion fluorescence in lateral roots (for *pMtAnn1:MtAnn1-GFP* and
542 *pENOD11:GFP-ER* constructs) or in the nucleus (for *p2x35S:NR-GECO1*). Selected composite
543 plants were then transferred to appropriate nitrogen- and antibiotic-free plates or pots for
544 subsequent inoculation with rhizobia.

545

546 **Plant growth and microbial inoculation procedures**

547 For *in vivo* imaging experiments, kanamycin-resistant and fluorescent-positive composite
548 plants of A17 (WT, *sunn-2*, *ern1*, *ern1 ern2* and *dmi3*) or R108 (R108S and *ann1-3*) carrying
549 *pMtAnn1:MtAnn1-GFP* + *p2x35S:NR-GECO1, pEXPA:NIN* + *pENOD11:GFP-ER* or *p2x35S:NR-*
550 *GECO1* + *pENOD11:GFP-ER* constructs were transferred to nitrogen-free Fahraeus plates
551 supplemented with Amoxycillin sodium/Clavulanate potassium 5:1 (200 mg/L) for 3-7 d, then

552 transferred to nitrogen-free 0.5% [w/v] phytagel Fahraeus plates supplemented with 50nM 2-
553 amino ethoxyvinyl glycine (AVG) for 3 days, as described previously[24]. Whole root systems
554 were then inoculated with 0.5 to 1 mL of the *Sm*2011-cCFP suspension (OD_{600nm} 0.001), applied
555 between the medium and the LUMOX film. The inoculated root systems were kept protected
556 from light, by wrapping ¾ of the plates with dark plastic bags in a culture room at 20°C or 25°C
557 with a 16-h photoperiod and a light intensity of 70 mE/s/m^2, until microscopy observations.

558 For high-resolution microscopy analyses of pre-infection priming in A17 and nodule
559 differentiation in WT/*ann-3*, germinated seedlings of *M. truncatula* A17 and R108 (R108S and
560 *ann1-3*) were grown for 3 days on nitrogen-free paper/Fahraeus Kalys HP696 agar plates[46]
561 before roots were either spot or flood-inoculated with water (control) or a *Sm*2011-LacZ
562 (OD_{600nm} 0.01) suspension, as described in[29]. For expression analyses of *pMtAnn1:GUS* (in
563 pLP100) in A17 and *nin* (co-expressing or not *pEXPA:NIN*), kanamycin-resistant and/or Ds-Red
564 fluorescence-positive composite plants were transferred 3 weeks after *A. rhizogenes*
565 transformation to the same nitrogen-free paper/Fahraeus Kalys HP696 agar plates and grown
566 for 3 days prior to flood inoculation (for 1h) of the entire root system with *Sm*2011-LacZ
567 (OD_{600nm} 0.01). Plants grown *in vitro* on plates were all cultivated at 25°C under a 16-h
568 photoperiod and a light intensity of 70 mE/s/m^2 with their root systems protected from light
569 by wrapping ¾ of the plates with dark plastic bags.

570 For phenotyping experiments, germinated seedlings of *M. truncatula* R108 lines (R108, R108S
571 and *ann1-1 to ann1-3* mutants), and selected composite plants (2-3 weeks after
572 transformation) of A17-transformed with MtAnn1-RNAi/control constructs or R108 (R108S or
573 *ann1-3*)-transformed with *p35S:GFP/p35S:MtAnn1-GFP* constructs, were transferred to 8 x 8
574 x 7cm pots (3 plants/pot for germinated seedlings and 2 plants/pot for composite plants) filled
575 with inert attapulgite substrate (Oil Dri US Special; http://www.oildri.com/), supplemented
576 with 10mL nitrogen-free Fahraeus medium. For longer growth periods (> 3 wpi), plants were
577 grown in 9 x 9 x 8 cm pots (3 plants/pot) supplemented with 14mL medium. Pots were placed
578 in small greenhouses at 25°C, with a 16 h photoperiod and a light intensity of 100 mE/s/m^2,
579 and inoculated with a suspension of *Sm*2011-LacZ (OD_{600nm} 0.1), after 3 days of nitrogen
580 starvation.

581 To assess mycorrhizal root colonization of WT and *ann1-3* mutant lines, germinated seedlings
582 were transferred to 8 x 8 x 7cm pots (1 plant per pot), filled with a 1:1 mix of Zeolite substrate
583 fractions 1.0-2.5 mm and 0.5-1.0 mm (Symbiom LTD, Lanskroun, Czech Republic), and
584 inoculated with *R. irregularis* spores (strain DAOM197198, 150 spores per pot). Pots were
585 placed in 60 x 40 x 12 cm trays in a 16 h photoperiod chamber (light intensity: 300 µmol/s/m^2)
586 at a day-time temperature of 22 °C and a night-time temperature of 20°C, and 70% humidity.
587 Plants were watered weekly with a modified low-phosphate and low-nitrogen Long Ashton
588 solution (7.5 µM Na_2HPO_4, 750 µM KNO_3, 400 µM $Ca(NO_3)_2$, 200 mg/L MES buffer, pH 6.5).

589

590 **β-glucuronidase (GUS) and β-galactosidase enzymatic assays**

591 Root segments from *M. truncatula* composite plants expressing *pMtAnn1:GUS* (in pLP100) or
592 *pEXPA:NIN + pMtAnn1:GUS* constructs were collected from control (water) or rhizobia-
593 inoculated roots and incubated in 0.5 % paraformaldehyde/0.1 M potassium phosphate buffer
594 pH 7.0, for 1 h, prior to histochemical (blue) staining for GUS activity for 2-5 hours at 37 °C
595 using 1 mM of the substrate X-Gluc (5-bromo-4-chloro-3-indoxyl-b-D-GlcA,
596 cyclohexylammonium salt, B7300; Biosynth, Staad, Switzerland) as described[50]. For

597 mycorrhizal roots expressing *pMtAnn1:GUS*, composite plants were harvested 4 weeks after
598 inoculation with *R. irregularis*. The root system was vacuum-infiltrated five times for 5 min
599 each with GUS staining solution (0.5 mg/ml X-Gluc, 100 mM phosphate buffer pH 7.0, 100 mM
600 EDTA, 0.5 mM $K_4[Fe(CN)_6]$, 0.5 mM $K_3[Fe(CN)_6]$ and 0.1% Triton X-100), and then incubated in
601 this solution for 1 h at 37 °C in the dark. Histochemical GUS staining of *N. benthamiana* leaf
602 discs was carried out in the same X-Gluc substrate but supplemented with 0,1 % triton, first
603 under vacuum for 20 min at room temperature before incubation at 37 °C for 3 h. Enzymatic
604 GUS fluorimetric assays of *N. benthamiana* leaf discs were done according to [45]. Briefly, tissues
605 were ground using a MM400 grinder (Retsch) and homogenized in GUS extraction buffer
606 before 1 µg of total protein extracts were used for enzymatic reactions at 37°C using 1 mM of
607 the 4-MUG substrate (4-Methylumbelliferyl-β-D-glucuronide hydrate, Biosynth M-5700). GUS
608 activity was measured using a FLUOstar Omega 96 microplate reader (BMG LABTECH, France)
609 through quantification of the fluorescence of 4-MU (4-Methylumbelliferone, Sigma) reaction
610 product. To reveal the constitutive β-galactosidase activity of the *S. meliloti* strain *Sm2011-*
611 *lacZ* in ITs, root samples (sometimes pre-stained for GUS activity) were rinsed and fixed for 1
612 h in 1.25 % glutaraldehyde/Z buffer (10 mM KCl, 1 mM $MgCl_2$, and 0.1 M phosphate buffer,
613 pH 7.0) as described[45]. After rinsing in Z-buffer, root samples were incubated overnight in the
614 dark at 28 °C in Z-buffer containing 2 mM Magenta-Gal (5-bromo-6-chloro-3-indoxyl-b-D-
615 galactopyranoside; B7200; Biosynth) or X-Gal (5-bromo-4-chloro-3-indolyl-b-D-
616 galactopyranoside, W5376C; Thermo Fisher Scientific, Guilford, CT). GUS and/or LacZ-stained
617 tissues were cleared for 30 s with 12 % sodium hypochlorite solution before microscopy
618 observations.

619

620 **Tissue harvesting and microscopy methods**

621 Roots of *M. truncatula* composite plants expressing different fluorescent fusions and grown
622 under LUMOX film were observed using a Leica TCS SP8 AOBS laser scanning confocal
623 microscope equipped with a 40x long distance water immersion objective (HCX APO L U-V-I
624 40x/0.80 WATER). Confocal images were recorded using Leica LAS-X software, before and
625 after rhizobia inoculation (from 1 to 7 dpi). For GFP, CFP and DsRed or mCherry fluorescent
626 proteins, 458 nm and 488 nm Argon laser lines and a 561 nm diode were used for excitation,
627 respectively, with emission windows set at 465-495 nm, 500-525 nm and 570-600 nm (DsRed)
628 or 600-630 nm (mCherry) (hybrid detector), respectively. To avoid potential interference,
629 sequential mode was used to acquire CFP and red fluorescent protein fluorescence separately
630 from GFP fluorescence and bright-field images. For confocal imaging of calcium responses, the
631 561 nm diode was used to excite the mApple red fluorescent protein from the NR-GECO1
632 sensor, and the emitted fluorescence was recovered using a hybrid detector in the 600 to 643
633 nm emission window. Time series (t-series) were acquired at 5 s intervals for 10 to 15 min,
634 with pinhole diameter set to 3 Airy units, as described[46].

635 Roots or nodulated roots of *M. truncatula* A17 and R108 (R108S and *ann1-3*) or composite
636 plants were selected based on their fluorescence and/or analyzed before or after GUS and/or
637 β-galactosidase staining using stereomicroscopy (Leica S6E) or light microscope (AxioPlan II
638 Imaging; Carl Zeiss, Oberkochen, Germany). For *pMtAnn1:GUS* (in pLP100) expression
639 analysis, samples were harvested 0 and 4 dpi with rhizobia. For comparative phenotyping of
640 wild-type and *MtAnn1* mutant or RNAi roots, β-galactosidase stained nodulated root samples
641 were harvested 4-5 or 8-10 dpi with rhizobia. Roots expressing *pEXPA:NIN* + *pMtAnn1:GUS*

642 were dehydrated in ethanol series and embedded in glycol methacrylate (Technovit 7100;
643 Haereus-Kulzer) according to the manufacturer's instructions. Sections of 10 µm were
644 counterstained with aqueous basic fushin solution (0.007%) for observations. To quantify
645 nodule size and rhizobia infection levels , β-galactosidase-stained nodulated root systems (10
646 dpi) from WT and *ann1-3* plants were scanned (Objectscan 1600, Microtek) and the acquired
647 images (TIFF) were used for image quantification (see details in the following part of the
648 methods).

649 For high-resolution microscopy analyses of pre-infection priming responses in A17, control
650 roots and rhizobia-infected root regions or nodule primordia were carefully isolated from
651 spot-inoculated or flood-inoculated root systems 5-6 dpi, after histochemical revelation of
652 rhizobial β-galactosidase activity. Harvested root sections or nodule primordia were fixed in
653 2% glutaraldehyde, diluted in 0.2 M cacodylate buffer pH=7.3 for a few hours at room
654 temperature or 1-3 days at 4°C, then rinsed with buffer, before progressive dehydration in an
655 ethanol series and final inclusion in LR White resin following manufacturer's instructions
656 (EMS). For comparative ultrastructural analysis of isolated R108S and *ann1-3* nodules, nodule
657 samples were carefully isolated from rhizobia-inoculated root systems 14-16 dpi and fixed
658 under vacuum in 2 successive batches of 2.5% glutaraldehyde diluted in 0.2 M cacodylate
659 buffer pH=7.3, the first batch containing saponin or triton (0.1 % final) for 3-5 days at 4°C.
660 After rinsing in buffer, post-fixation in 2% osmium tetroxyde (diluted in 0.2 M sodium
661 cacodylate), rinsing again in buffer, progressive dehydration in an ethanol series and
662 incubation in propylene oxide (2 x 1h), samples were finally embedded in Epon 812 resin (EMS)
663 following the manufacturer's instructions. For all samples, semi-thin (1 µm) and ultra-thin (80
664 nm) sections were generated using an Ultracut E ultramicrotome (Reichert Jung). Semi-thin
665 sections of root/nodule primordia (5-6 dpi) were stained with basic fuchsin (0.07 % in water)
666 to help visualize ITs, while mature nodule sections (14-16 dpi) were stained in an aqueous
667 solution with methylene blue (0.2 %), toluidine blue (1 %), borax (1 %) and basic fuchsin (0.07
668 %) before observation by bright field microscopy (Axioplan II Imaging; Carl Zeiss). Ultrathin
669 sections (80 nm) were contrasted with Uranyless and lead citrate (Delta microscopy) and
670 observed using a Hitachi 7700 electron microscope (Hitachi High-Tech).

671 For histochemical GUS staining of mycorrhizal roots, selected composite plants transformed
672 with *pMtAnn1:GUS* were transferred to 7 x 7 x 8 cm pots (5 plants/pot) filled with washed
673 quartz sand (grain size 0.7-1.2 mm) pre-watered with modified half-strength Hoagland
674 solution containing 20 µM phosphate[79]. Each plant was inoculated with 500 spores of *R.*
675 *irregularis* DAOM197198 (C-grade, Agronutrition, Toulouse, France). Plants were grown in a
676 Polyklima cabinet at 22°C constant temperature, 60 % air humidity and 16-h-light/8-h-dark
677 cycles, at 200 µE/s/m2 light intensity and a combination of warm and cold LED 'True DayLight'
678 at a 40:25 ratio. Pots were watered twice per week with 30-40 ml of autoclaved de-ionized
679 tap water and fertilized once per week with 30-40 ml of modified half-strength Hoagland
680 solution containing 20 µM phosphate. To visualize the fungal structures, the GUS staining
681 solution was exchanged for 10 % KOH and the roots incubated for 15 min at 95°C. After KOH
682 removal, the roots were washed 3 times with de-ionized water. After addition of 0.1 M HCl,
683 the roots were further incubated for 2 h in the dark at room temperature. HCl was removed
684 and the roots were washed 3 times with de-ionized water and once with PBS. This was
685 followed by an overnight incubation at room temperature in the dark with 200 ng/µL WGA
686 Alexa Fluor 488 (Invitrogen W11261) in PBS. Roots were imaged with a LEICA DM6B
687 epifluorescence microscope. To compare the extent of mycorrhizal colonization of roots

688 between WT and *ann1-3* lines, whole root systems were collected 6 weeks post-inoculation
689 with *R. irregularis* and cleared by boiling (95°C) in 10% KOH for 5 minutes, rinsed with water,
690 then stained by boiling in an acidic ink solution (5% acetic acid, 5% Sheaffer black ink #94321,
691 in water) to reveal fungal structures. Overall intraradical colonization rates and arbuscular
692 density were estimated in ink-stained roots under a stereomicroscope (Leica S6E) using the
693 gridline intersect method.

694

695 **Microscopy image analyses**

696 Analysis of confocal t-series was performed using the Fiji software[80]. Intensity data were
697 calculated from selected regions of interest (ROIs), corresponding to single nuclei, imaged in
698 independent roots, in 2-3 independent experiments. Maximal z-projections of stacks and
699 merged confocal images for illustration purpose were prepared using Leica confocal software
700 or Fiji. To quantify relative amplitudes of Ca^{2+} spiking, the mean fluorescence of each ROI was
701 measured as a function of time and used to determine the Signal-to-Noise Ratio (SNR). The
702 SNR measures the difference between the fluorescence at each time-point (F_t) and the
703 fluorescence baseline, calculated as the average of 4 fluorescence values taken 10 and 15 sec
704 before and after t (F_{t-15}; F_{t-10}; F_{t+10}; F_{t+15}). A threshold of 0.3 was applied to the SNR to define
705 individual peaks, and the amplitude of Ca^{2+} spiking was calculated for each nucleus as the mean
706 of peak SNR values. Spiking frequency, defined as the number of peaks observed in 10 min,
707 was also calculated. In each experiment where calcium spiking was monitored, nuclei
708 displaying no spiking were also included, resulting in the sample size (n) being higher in the
709 frequency graph than in the associated amplitude graph.

710 For quantification of MtAnn1-GFP fluorescence levels, root hairs were imaged at either the
711 RHE or IT stages with identical acquisition settings in 3 independent experiments. In each
712 acquired confocal z-stack, 4 to 6 successive confocal sections encompassing the cytoplasmic
713 aggregation around the site of rhizobia entrapment (RHE) or the cytoplasmic bridge
714 characteristic of the IT stage were selected. In ImageJ, the threshold function was used to
715 generate a mask based on a maximal z-projection of the selected sub-stack, from which the
716 contours of the cytoplasmic zone (ROI) were defined. The mean grey value was then measured
717 in the defined ROI on an average z-projection of the same sub-stack.

718 Scanned images of β-galactosidase-stained root systems from R108S and *ann1* mutants (10
719 dpi) were imported to Ilastik software[87] to enable machine-learning recognition of blue β-
720 galactosidase-stained nodules (pixel-based classification method). Objects identified as
721 nodules were exported in a new single segmentation .tiff file for analysis in ImageJ to measure
722 specific nodule features (size and infection level, based on the blue intensity of rhizobial β-
723 galactosidase activity).

724

725 **Transient expression assays in *N. benthamiana* leaves**

726 An *A. tumefaciens* GV3101 strain carrying the *pMtAnn1:GUS* fusion construct (in pLP100) was
727 used for infiltration studies in *N. benthamiana* alone or with *A. tumefaciens* GV3103 strains
728 carrying *p35S:NIN* or *p35S:NINΔ* constructs[52], designed to constitutively express NIN or NINΔ
729 under the 35S promoter in transactivation experiments. Briefly, *A. tumefaciens* strains grown
730 overnight at 28°C in LB medium with appropriate antibiotics were harvested and resuspended
731 in Agromix (10 mM $MgCl_2$, 10 mM MES/KOH pH 5.6 and Acetosyringone in DMSO Sigma-

732 Aldrich 150 µM) and kept in the dark for at least 2h, at room temperature. Equal volumes of
733 *A. tumefaciens* cultures (OD_{600}=0.25) were used to co-infiltrate leaf discs of 3-week-old *N.*
734 *benthamiana* plants. Infiltrated plants were kept at 21°C in a growth chamber (16-h
735 photoperiod and a light intensity of 70 mE/s/m2) for 36 h prior to histochemical GUS assays
736 or storage at -70°C prior to protein extraction for Western-blot or fluorimetric GUS assays.

737

738 **Western blot analyses**

739 *N. benthamiana* leaf discs, previously stored at -80°C, were ground using a MM400 (Retsch)
740 crusher and resuspended in Laemmli 2X sample buffer for SDS-PAGE (Bio-rad). Samples were
741 then placed at 95°C for 3 min and centrifuged at 13200 rpm for 1 min. For each sample, 10 µL
742 of the supernatant was loaded in a polyacrylamide 4-15% Mini-PROTEAN precast gel (Bio-Rad)
743 along with 5 µL of pre-stained protein ladder marker (ThermoScientific, Lithuania). The Mini-
744 Protean tank Electrophoresis System (Biorad, USA) was used for gel migration in 1 X
745 Tris/Glycine/SDS Buffer (Bio-Rad). Protein transfer to nitrocellulose membranes (Bio-Rad) was
746 performed using a Trans-Blot Turbo semi-dry transfer system (Bio-Rad). Membranes were
747 stained with Ponceau Red before incubation for 1 h in blocking 1 x TBS solution (Tris base,
748 NaCl and H_2O), 0.1 % Tween, 5 % milk at room temperature, with mild agitation, before rinsing
749 3 x in TBS-Tween 0.1 % for 10 min, and incubated overnight in the same solution at 4°C with a
750 6000 X dilution of anti-HA-peroxidase antibodies (Sigma-Aldrich) in 0.5 % milk in TBS-Tween
751 0.1 % to reveal HA-tagged NIN proteins following chemiluminescence revelation using the
752 Clarity Western ECL Substrate (Bio-Rad) and the ChemiDoc Touch imaging system (Bio-Rad).

753

754 **Acetylene reduction assay**

755 To assess nitrogenase activity, grouped nodules were isolated from root systems of plants
756 grown in pots 3 weeks after inoculation with *Sm*2011-LacZ and tested for acetylene reduction.
757 Nodulated root fragments were incubated at 25°C in sealed 60 mL vials containing 0.5 mL of
758 nitrogen-free Fahraeus liquid medium in the presence of 10 % (v/v) acetylene for 3 h. 400 µL
759 of gaz was then collected from each vial and ethylene production was quantified by gas
760 chromatography (model no. GC 7280A; Agilent Technologies, Lexington, MA).

761

762 **RNA extraction and quantitative RT-PCR analysis**

763 Total RNA was extracted from *M. truncatula* control and rhizobia-inoculated roots (4-5 dpi)
764 using the Macherey-Nagel total RNA isolation kit according to the manufacturer's instructions.
765 DNA-free RNA samples were quantified, and RNA integrity was verified by Agilent RNA Nano
766 Chip (Agilent Technologies). First-strand complementary DNA synthesis was performed using
767 1 µg of total RNA using an anchored oligo (dT) and Transcriptor Reverse Transcriptase (Roche)
768 following the manufacturers' protocol. Quantitative RT-PCR was performed on 384-well
769 plates, with Light Cycler 480 systems fromRoche or Biorad and using the SYBR Green I Master
770 mixes (Roche or Takyon, Eurogentec), according to manufacturer's instructions. Reactions and
771 cycling conditions were performed as described before[29] using Primer pairs listed in
772 Supplementary Table S1. The specificity of the PCR amplification was verified by analysing the
773 PCR dissociation curve and sequencing of the PCR product. Transcript levels were normalized
774 to the endogenous Ubiquitin reference.

775

776 **Phylogenetic analysis**

777 Protein sequence of *MtAnn1* (MtrunA17_Chr8g0352611) was used as query to search against
778 a database containing 227 plant genomes covering the main lineages of green plants and five
779 SAR genomes as outgroups using the BLASTp v2.14.0+ with an e-value threshold of 1e-10[55].
780 Homologous proteins were then aligned using Muscle v5.1 with the "super5" option[82] and
781 trimmed to remove positions with more than 60% of gaps using trimAl v1.4.rev22[83]. The
782 trimmed alignment served as matrix for phylogenetic reconstruction using FastTree v2.1.11-
783 OpenMP[84]. To gain insights about the evolution of Ann1 in relation with the nitrogen-fixing
784 symbiosis, the flowering clade corresponding containing orthologs of MtAnn1 has been
785 extracted and proteins re-aligned using Muscle with default parameters before trimming as
786 described above. Few spurious sequences with obvious mispositioning and abnormal short
787 sequences were removed. Then, maximum likelihood tree has been reconstructed using IQ-
788 TREE v2.1.2[85] after testing the best evolution model using ModelFinder[86] as implemented in
789 IQ-TREE2 and according to the Bayesian Information Criteria. Branch supports have been
790 tested with 10,000 replicates of both SH-aLRT[87] and UltraFast Bootstraps with UFBoot2[88].
791 Finally, trees were visualized and annotated in the iTOL platform v6.8.1[89].

792

793 **Graph generation and statistical analyses**

794 Graph preparation and statistical analyses were performed using R (http://r-project.org),
795 except for graphs in Fig. 5C and D, which were generated using Microsoft Excel and for which
796 contingency analyses were performed using GraphPad Prism 10. For all other analyses, data
797 were presented as boxplots, normal distribution of the data was evaluated using the Shapiro-
798 Wilk test, and homogeneity of variance was assessed using Fisher or Bartlett tests. When
799 applicable, a transformation was performed to normalize data distribution (Log10 or BoxCox).
800 Parametric statistical tests (t-test, ANOVA) were used to analyze data with a normal
801 distribution, while non-parametric equivalents (Mann-Whitney, Kruskal-Wallis) were used for
802 data with a non-normal distribution. Number of individually analyzed samples (n), replicates
803 and *p* significance levels are indicated in Figure legends. In detail, data was analyzed as follows:
804 Fig. 2: values in Fig. 2E follow a normal distribution and display homogeneous variance, so a
805 two-tailed Student t-test was performed (t=-3.0927, df=39, p=0.0037); values in Fig. 2F do not
806 follow a normal distribution and were thus analyzed using a two-tailed Mann-Whitney test
807 (W=315, p=0.1531). Fig. 4: Log10-transformed values in Fig. 4G follow a normal distribution
808 and variance homogeneity and were thus analyzed using one-way ANOVA followed by Tukey
809 honest significant difference (HSD) tests (F=149.5, df=2, p<2e-16). Fig. 5: Values in Fig. 5A and
810 5B do not follow a normal distribution, hence Kruskal-Wallis tests were carried out (K=6.499,
811 p= 0.0388 for A, and K= 6.204, p=0.0449 for B). Fig. 5C and 5D were built from contingency
812 tables reporting numbers of nodule primordia belonging to different categories: fully infected
813 (+) or poorly infected or not infected (+/- or -) in C, or NPs with a sole IT extended to the cortex
814 (1 IT) or several ITs (≥ 2 ITs) in D. Relative proportions of these categories were compared one-
815 on-one between R108S and each other genotypes (R108, *ann1-2* and *ann1-3*), by running
816 separate Fisher's exact tests. Results of said tests are (C) R108S vs R108 p=0. 0,2738, R108S vs

ann1-2 p< 0,0077, R108S vs *ann1-3* p= 0,0428, and (D) R108S vs R108 p=0.4432, R108S vs *ann1-2* p=0.0128, R108S vs *ann1-3* p=0.0007. Values in Fig. 5O follow a normal distribution and variance homogeneity and were thus analyzed using one-way ANOVA followed by Tukey honest significant difference (HSD) tests (F=180,81, df=3, p<0,076), and values in 5P do not follow a normal distribution and were thus analyzed by a Kruskal-Wallis test (K=55.44 and p<0.0001). In Fig. 5Q, values follow a normal distribution and variance homogeneity, hence a two-tailed Student t-test was carried out (t=2.4153, df=99, p=0.0176), while values in Fig. 5R do not follow a normal distribution, thus two-tailed Mann-Whitney tests were applied (W=1724, p=0.0023). Fig. 6: Values in Fig. 6P follow a normal distribution but not homogeneity of variances, thus a Welsh two-sample t-test was carried out (t=4.8433, df=8.2905, p=0.0012). Log10-transformed values in Fig. 6Q show a normal distribution and variance homogeneity and were thus analyzed using a two-tailed Student t-test (t=-3.066, df=27, p=0.0049). Fig. 7: Values in Fig. 7A-B, which show a normal distribution and variance homogeneity were analyzed using one-tailed Student t-tests, due to the low number of values (7A: t=2.1821, df=9, p=0.0285; 7B: t=0.9612, df=22, p=0.1735). In Fig. 7C, values do not follow a normal distribution, thus a two-tailed Mann-Whitney test was performed (W=9944, p=0.0018). Fig. 8: In Fig. 8, values in 8I and BoxCox-transformed values in 8J (λ=1.353535) show a normal distribution and homogeneity of variance and were thus analyzed using two-tailed Student t-test (8I: t=3.6816, df=72, p=0.00045; 8J: t=3.8831, df=72, p=0.0002). Distribution of values is not normal in Fig. 8K, so data was analyzed via a Mann Whitney test (W=9103, p=0.0046.) Log-transformed values of Fig. 8L follow a normal distribution so a two-tailed Student t-test was applied (t=2.758, df=17, p=0.0134). Supplementary Fig. S1: In Fig. S1B, values do not follow a normal distribution, thus a Mann Whitney test was carried out (W=35, p=0.005349), while in Fig. S1C values do show a normal distribution, so a two-tailed Student t-test was performed (t=3.9724, df=10, p=0.0026). In Supplementary Fig. S2E-H, values show a non-normal distribution and were thus analyzed using two-tailed Mann-Whitney tests (S2E: W=853, p=1.811e-07; S2F: W=205, p=2.893e-05, S2G: W=348, p=3.377e-09, S2H: W=237, p=1.926e-09). In Supplementary Fig. S7C, values follow a normal distribution, hence a two-tailed Student t-test was performed (t=1.9307, df=6, p=0.1017). In Supplementary Fig. S12B and S12C, Log-transformed data follow a normal distribution, so one-way ANOVAs followed by Tukey honest significant difference (HSD) tests were carried out (respectively F=321.1, df=9, p<2e-16 for B, and F=1.701, df=9, p=0.106 for C). Log-transformed data in Fig. S12D, and non-transformed data in Fig. S12E follow a normal distribution, hence two-tailed Student t-tests were employed (respectively t=4.4053, df=22, p=0.0002 for D, and t=2.0775, df=22, p=0.0496 for E). In Fig. S12F, values do not have a normal distribution, so a Kruskal-Wallis test was used (K=43.0318, p=4.5265e-10). In Fig. S12G, data follows a normal distribution, so a one-way ANOVA followed by Tukey honest significant difference (HSD) tests was carried out (F=4.593, df=2, p=0.0143). In Supplementary Fig. S13C and S13E, data follow a normal distribution (after a Log-transformation for S13C), hence one-way ANOVAs followed by Tukey honest significant difference (HSD) tests were used for comparisons (respectively F=2.223, df=4, p=0.0765 for S13C and F=4.398, df=4, p=0.0034 for S13E). Values in Fig. S13D do not follow a normal

858 distribution, so statistical analysis was done using a Kruskal-Wallis test (K=9.15, p=0.0575). In
859 Supplementary Fig. S15C and S15E, values do not follow a normal distribution and were thus
860 analyzed using two-tailed Mann-Whitney tests (Respectively W=18215, p=0.3726 for S15C,
861 and W=86, p=0.57 for S15E), while values in S15D do follow a normal distribution and variance
862 homogeneity, and were analyzed using a two-tailed Student t-test (t=-1.0271, df=10,
863 p=0.3286).

864

865 **Reporting summary**. Further information on research design is available in the Nature
866 Research Reporting Summary linked to this article.

867

868 **Data availability**

869 The authors declare that all data supporting the results of this study are available within the
870 article and its Supplementary Information Files. Materials generated in this study are available
871 from the corresponding authors upon request.

872

873 **References**

874 1 Lanfranco, L., Fiorilli, V. & Gutjahr, C. Partner communication and role of nutrients in the
875 arbuscular mycorrhizal symbiosis. *New Phytol* **220**, 1031-1046 (2018).
876 https://doi.org/10.1111/nph.15230
877 2 Huisman, R. & Geurts, R. A Roadmap toward Engineered Nitrogen-Fixing Nodule Symbiosis.
878 *Plant Commun* **1**, 100019 (2020). https://doi.org/10.1016/j.xplc.2019.100019
879 3 Genre, A. & Russo, G. Does a Common Pathway Transduce Symbiotic Signals in Plant-Microbe
880 Interactions? *Front Plant Sci* **7**, 96 (2016). https://doi.org/10.3389/fpls.2016.00096
881 4 Griesmann, M. *et al.* Phylogenomics reveals multiple losses of nitrogen-fixing root nodule
882 symbiosis. *Science* **361** (2018). https://doi.org/10.1126/science.aat1743
883 5 Libourel, C. *et al.* Comparative phylotranscriptomics reveals ancestral and derived root nodule
884 symbiosis programmes. *Nat Plants* **9**, 1067-1080 (2023). https://doi.org/10.1038/s41477-023-
885 01441-w
886 6 Charpentier, M. Calcium Signals in the Plant Nucleus: Origin and Function. *J Exp Bot* (2018).
887 https://doi.org/10.1093/jxb/ery160
888 7 Krönauer, C. & Radutoiu, S. Understanding Nod factor signalling paves the way for targeted
889 engineering in legumes and non-legumes. *Curr Opin Plant Biol* **62**, 102026 (2021).
890 https://doi.org/10.1016/j.pbi.2021.102026
891 8 Lévy, J. *et al.* A putative Ca2+ and calmodulin-dependent protein kinase required for bacterial
892 and fungal symbioses. *Science* **303**, 1361-1364 (2004).
893 https://doi.org/10.1126/science.1093038
894 9 Tirichine, L. *et al.* Deregulation of a Ca2+/calmodulin-dependent kinase leads to spontaneous
895 nodule development. *Nature* **441**, 1153-1156 (2006). https://doi.org/10.1038/nature04862
896 10 Singh, S., Katzer, K., Lambert, J., Cerri, M. & Parniske, M. CYCLOPS, a DNA-binding
897 transcriptional activator, orchestrates symbiotic root nodule development. *Cell Host Microbe*
898 **15**, 139-152 (2014). https://doi.org/10.1016/j.chom.2014.01.011
899 11 Cerri, M. R. *et al.* The ERN 1 transcription factor gene is a target of the CC a MK/CYCLOPS
900 complex and controls rhizobial infection in Lotus japonicus. *New Phytologist* **215**, 323-337
901 (2017).
902 12 Pimprikar, P. & Gutjahr, C. Transcriptional Regulation of Arbuscular Mycorrhiza Development.
903 *Plant and Cell Physiology* **59**, 678-695 (2018). https://doi.org/10.1093/pcp/pcy024

13 De Carvalho-Niebel, F., Timmers, A. C., Chabaud, M., Defaux-Petras, A. & Barker, D. G. The Nod factor-elicited annexin MtAnn1 is preferentially localised at the nuclear periphery in symbiotically activated root tissues of Medicago truncatula. *Plant J* **32**, 343-352 (2002).
14 Manthey, K. *et al.* Transcriptome profiling in root nodules and arbuscular mycorrhiza identifies a collection of novel genes induced during Medicago truncatula root endosymbioses. *Mol Plant Microbe Interact* **17**, 1063-1077 (2004). https://doi.org/10.1094/MPMI.2004.17.10.1063
15 Davies, J. M. Annexin-Mediated Calcium Signalling in Plants. *Plants (Basel)* **3**, 128-140 (2014). https://doi.org/10.3390/plants3010128
16 Gerke, V. *et al.* Annexins-a family of proteins with distinctive tastes for cell signaling and membrane dynamics. *Nat Commun* **15**, 1574 (2024). https://doi.org/10.1038/s41467-024-45954-0
17 Gutjahr, C. & Parniske, M. Cell and developmental biology of arbuscular mycorrhiza symbiosis. *Annu Rev Cell Dev Biol* **29**, 593-617 (2013). https://doi.org/10.1146/annurev-cellbio-101512-122413
18 de Carvalho-Niebel, F., Fournier, J., Becker, A. & Marín Arancibia, M. Cellular insights into legume root infection by rhizobia. *Curr Opin Plant Biol* **81**, 102597 (2024). https://doi.org/10.1016/j.pbi.2024.102597
19 Gao, J. P., Liang, W., Liu, C. W., Xie, F. & Murray, J. D. Unraveling the rhizobial infection thread. *J Exp Bot* (2024). https://doi.org/10.1093/jxb/erae017
20 Roth, R. *et al.* Arbuscular cell invasion coincides with extracellular vesicles and membrane tubules. *Nat Plants* **5**, 204-211 (2019). https://doi.org/10.1038/s41477-019-0365-4
21 Ivanov, S., Austin, J., Berg, R. H. & Harrison, M. J. Extensive membrane systems at the host-arbuscular mycorrhizal fungus interface. *Nat Plants* **5**, 194-203 (2019). https://doi.org/10.1038/s41477-019-0364-5
22 Xiao, T. T. *et al.* Fate map of Medicago truncatula root nodules. *Development* **141**, 3517-3528 (2014). https://doi.org/10.1242/dev.110775
23 Gaudioso-Pedraza, R. *et al.* Callose-Regulated Symplastic Communication Coordinates Symbiotic Root Nodule Development. *Curr Biol* **28**, 3562-3577.e3566 (2018). https://doi.org/10.1016/j.cub.2018.09.031
24 Lin, J., Frank, M. & Reid, D. No Home without Hormones: How Plant Hormones Control Legume Nodule Organogenesis. *Plant Commun* **1**, 100104 (2020). https://doi.org/10.1016/j.xplc.2020.100104
25 Chaulagain, D. & Frugoli, J. The Regulation of Nodule Number in Legumes Is a Balance of Three Signal Transduction Pathways. *Int J Mol Sci* **22** (2021). https://doi.org/10.3390/ijms22031117
26 Fournier, J. *et al.* Remodeling of the infection chamber before infection thread formation reveals a two-step mechanism for rhizobial entry into the host legume root hair. *Plant physiology* **167**, 1233--1242 (2015). https://doi.org/10.1104/pp.114.253302
27 Su, C. *et al.* Transcellular progression of infection threads in Medicago truncatula roots is associated with locally confined cell wall modifications. *Curr Biol* **33**, 533-542.e535 (2023). https://doi.org/10.1016/j.cub.2022.12.051
28 Liu, C. W. *et al.* A protein complex required for polar growth of rhizobial infection threads. *Nat Commun* **10**, 2848 (2019). https://doi.org/10.1038/s41467-019-10029-y
29 Lace, B. *et al.* RPG acts as a central determinant for infectosome formation and cellular polarization during intracellular rhizobial infections. *Elife* **12** (2023). https://doi.org/10.7554/eLife.80741
30 Li, X. *et al.* RPG interacts with E3-ligase CERBERUS to mediate rhizobial infection in Lotus japonicus. *PLoS Genet* **19**, e1010621 (2023). https://doi.org/10.1371/journal.pgen.1010621
31 Breakspear, A. *et al.* The root hair "infectome" of Medicago truncatula uncovers changes in cell cycle genes and reveals a requirement for Auxin signaling in rhizobial infection. *Plant Cell* **26**, 4680-4701 (2014). https://doi.org/10.1105/tpc.114.133496

954 32 Gao, J. P. *et al.* Intracellular infection by symbiotic bacteria requires the mitotic kinase
955 AURORA1. *Proc Natl Acad Sci U S A* **119**, e2202606119 (2022).
956 https://doi.org/10.1073/pnas.2202606119
957 33 Yang, W. C. *et al.* Rhizobium nod factors reactivate the cell cycle during infection and nodule
958 primordium formation, but the cycle is only completed in primordium formation. *Plant Cell* **6**,
959 1415-1426 (1994). https://doi.org/10.1105/tpc.6.10.1415
960 34 Batzenschlager Morgane1, Lace Beatrice1, Zhang Ning1,2, Su Chao1, Egli Sabrina1, Krohn
961 Pascal1,3,4 & Salfeld Jule1, D. F. A., 4, Laux Thomas1,2, and Ott Thomas1,2,*. (bioRxiv, 2023).
962 35 Fournier, J. *et al.* Mechanism of infection thread elongation in root hairs of Medicago
963 truncatula and dynamic interplay with associated rhizobial colonization. *Plant Physiol* **148**,
964 1985-1995 (2008). https://doi.org/10.1104/pp.108.125674
965 36 Perrine-Walker, F. M., Lartaud, M., Kouchi, H. & Ridge, R. W. Microtubule array formation
966 during root hair infection thread initiation and elongation in the Mesorhizobium-Lotus
967 symbiosis. *Protoplasma* **251**, 1099-1111 (2014). https://doi.org/10.1007/s00709-014-0618-z
968 37 van Brussel, A. A. *et al.* Induction of pre-infection thread structures in the leguminous host
969 plant by mitogenic lipo-oligosaccharides of Rhizobium. *Science* **257**, 70-72 (1992).
970 https://doi.org/10.1126/science.257.5066.70
971 38 Timmers, A. C., Auriac, M. C. & Truchet, G. Refined analysis of early symbiotic steps of the
972 Rhizobium-Medicago interaction in relationship with microtubular cytoskeleton
973 rearrangements. *Development* **126**, 3617-3628 (1999).
974 39 Berg, R. W. Vol. 77 1351–1357 (Can. J. Bot., 1999).
975 40 Genre, A., Chabaud, M., Faccio, A., Barker, D. G. & Bonfante, P. Prepenetration apparatus
976 assembly precedes and predicts the colonization patterns of arbuscular mycorrhizal fungi
977 within the root cortex of both Medicago truncatula and Daucus carota. *Plant Cell* **20**, 1407-
978 1420 (2008). https://doi.org/10.1105/tpc.108.059014
979 41 Genre, A., Ortu, G., Bertoldo, C., Martino, E. & Bonfante, P. Biotic and abiotic stimulation of
980 root epidermal cells reveals common and specific responses to arbuscular mycorrhizal fungi.
981 *Plant Physiol* **149**, 1424-1434 (2009). https://doi.org/10.1104/pp.108.132225
982 42 Russo, G. & Genre, A. Divide and Be Conquered-Cell Cycle Reactivation in Arbuscular
983 Mycorrhizal Symbiosis. *Front Plant Sci* **12**, 753265 (2021).
984 https://doi.org/10.3389/fpls.2021.753265
985 43 Sieberer, B. J., Chabaud, M., Fournier, J., Timmers, A. C. & Barker, D. G. A switch in Ca2+ spiking
986 signature is concomitant with endosymbiotic microbe entry into cortical root cells of Medicago
987 truncatula. *Plant J* **69**, 822-830 (2012). https://doi.org/10.1111/j.1365-313X.2011.04834.x
988 44 Takeda, N., Maekawa, T. & Hayashi, M. Nuclear-localized and deregulated calcium- and
989 calmodulin-dependent protein kinase activates rhizobial and mycorrhizal responses in Lotus
990 japonicus. *Plant Cell* **24**, 810-822 (2012). https://doi.org/10.1105/tpc.111.091827
991 45 Cerri, M. R. *et al.* Medicago truncatula ERN transcription factors: regulatory interplay with
992 NSP1/NSP2 GRAS factors and expression dynamics throughout rhizobial infection. *Plant*
993 *Physiol* **160**, 2155-2172 (2012). https://doi.org/10.1104/pp.112.203190
994 46 Kelner, A., Leitão, N., Chabaud, M., Charpentier, M. & de Carvalho-Niebel, F. Dual Color Sensors
995 for Simultaneous Analysis of Calcium Signal Dynamics in the Nuclear and Cytoplasmic
996 Compartments of Plant Cells. *Front Plant Sci* **9**, 245 (2018).
997 https://doi.org/10.3389/fpls.2018.00245
998 47 Wais, R. J., Keating, D. H. & Long, S. R. Structure-function analysis of nod factor-induced root
999 hair calcium spiking in Rhizobium-legume symbiosis. *Plant Physiol* **129**, 211-224 (2002).
1000 https://doi.org/10.1104/pp.010690
1001 48 Middleton, P. H. *et al.* An ERF transcription factor in Medicago truncatula that is essential for
1002 Nod factor signal transduction. *Plant Cell* **19**, 1221-1234 (2007).
1003 https://doi.org/10.1105/tpc.106.048264

1004 49 Andriankaja, A. *et al.* AP2-ERF transcription factors mediate Nod factor--dependent Mt
1005 ENOD11 activation in root hairs via a novel cis-regulatory motif. *The Plant Cell* **19**, 2866--2885
1006 (2007).
1007 50 Cerri, M. R. *et al.* The Symbiosis-Related ERN Transcription Factors Act in Concert to Coordinate
1008 Rhizobial Host Root Infection. *Plant Physiol* **171**, 1037-1054 (2016).
1009 https://doi.org/10.1104/pp.16.00230
1010 51 Rival, P. *et al.* Epidermal and cortical roles of NFP and DMI3 in coordinating early steps of
1011 nodulation in Medicago truncatula. *Development* **139**, 3383-3391 (2012).
1012 https://doi.org/10.1242/dev.081620
1013 52 Schiessl, K. *et al.* NODULE INCEPTION Recruits the Lateral Root Developmental Program for
1014 Symbiotic Nodule Organogenesis in Medicago truncatula. *Curr Biol* **29**, 3657-3668.e3655
1015 (2019). https://doi.org/10.1016/j.cub.2019.09.005
1016 53 Vernie, T. *et al.* The NIN Transcription Factor Coordinates Diverse Nodulation Programs in
1017 Different Tissues of the Medicago truncatula Root. *Plant Cell* **27**, 3410-3424 (2015).
1018 https://doi.org/10.1105/tpc.15.00461
1019 54 Liu, H. *et al.* A genetic screen for plant mutants with altered nodulation phenotypes in
1020 response to rhizobial glycan mutants. *New Phytol* **220**, 526-538 (2018).
1021 https://doi.org/10.1111/nph.15293
1022 55 Vasse, J., de Billy, F., Camut, S. & Truchet, G. Correlation between ultrastructural
1023 differentiation of bacteroids and nitrogen fixation in alfalfa nodules. *J Bacteriol* **172**, 4295-4306
1024 (1990). https://doi.org/10.1128/jb.172.8.4295-4306.1990
1025 56 de Carvalho Niebel, F., Lescure, N., Cullimore, J. V. & Gamas, P. The Medicago truncatula
1026 MtAnn1 gene encoding an annexin is induced by Nod factors and during the symbiotic
1027 interaction with Rhizobium meliloti. *Molecular plant-microbe interactions* **11**, 504--513 (1998).
1028 57 Radhakrishnan, G. V. *et al.* An ancestral signalling pathway is conserved in intracellular
1029 symbioses-forming plant lineages. *Nat Plants* **6**, 280-289 (2020).
1030 https://doi.org/10.1038/s41477-020-0613-7
1031 58 Clark, G. B., Morgan, R. O., Fernandez, M. P. & Roux, S. J. Evolutionary adaptation of plant
1032 annexins has diversified their molecular structures, interactions and functional roles. *New*
1033 *Phytol* **196**, 695-712 (2012). https://doi.org/10.1111/j.1469-8137.2012.04308.x
1034 59 Floss, D. S. *et al.* A Transcriptional Program for Arbuscule Degeneration during AM Symbiosis
1035 Is Regulated by MYB1. *Curr Biol* **27**, 1206-1212 (2017).
1036 https://doi.org/10.1016/j.cub.2017.03.003
1037 60 Seguí-Simarro, J. M., Coronado, M. J. & Staehelin, L. A. The mitochondrial cycle of Arabidopsis
1038 shoot apical meristem and leaf primordium meristematic cells is defined by a perinuclear
1039 tentaculate/cage-like mitochondrion. *Plant Physiol* **148**, 1380-1393 (2008).
1040 https://doi.org/10.1104/pp.108.126953
1041 61 Costa, A., Navazio, L. & Szabo, I. The contribution of organelles to plant intracellular Calcium
1042 signalling. *J Exp Bot* (2018). https://doi.org/10.1093/jxb/ery185
1043 62 Cui, Y. *et al.* A whole-cell electron tomography model of vacuole biogenesis in Arabidopsis root
1044 cells. *Nat Plants* **5**, 95-105 (2019). https://doi.org/10.1038/s41477-018-0328-1
1045 63 Cui, Y., Zhao, Q., Hu, S. & Jiang, L. Vacuole Biogenesis in Plants: How Many Vacuoles, How Many
1046 Models? *Trends Plant Sci* **25**, 538-548 (2020). https://doi.org/10.1016/j.tplants.2020.01.008
1047 64 Viotti, C. ER and vacuoles: never been closer. *Front Plant Sci* **5**, 20 (2014).
1048 https://doi.org/10.3389/fpls.2014.00020
1049 65 Evans, R. C. & Blackwell, K. T. Calcium: amplitude, duration, or location? *Biol Bull* **228**, 75-83
1050 (2015). https://doi.org/10.1086/BBLv228n1p75
1051 66 Whalley, H. J. & Knight, M. R. Calcium signatures are decoded by plants to give specific gene
1052 responses. *New Phytol* **197**, 690-693 (2013). https://doi.org/10.1111/nph.12087
1053 67 Xu, T., Niu, J. & Jiang, Z. Sensing Mechanisms: Calcium Signaling Mediated Abiotic Stress in
1054 Plants. *Front Plant Sci* **13**, 925863 (2022). https://doi.org/10.3389/fpls.2022.925863

68 Wais, R. J. *et al.* Genetic analysis of calcium spiking responses in nodulation mutants of Medicago truncatula. *Proc Natl Acad Sci U S A* **97**, 13407-13412 (2000). https://doi.org/10.1073/pnas.230439797

69 Marsh, J. F. *et al.* Medicago truncatula NIN is essential for rhizobial-independent nodule organogenesis induced by autoactive calcium/calmodulin-dependent protein kinase. *Plant Physiol* **144**, 324-335 (2007). https://doi.org/10.1104/pp.106.093021

70 Del Cerro, P. *et al.* Engineered CaM2 modulates nuclear calcium oscillation and enhances legume root nodule symbiosis. *Proc Natl Acad Sci U S A* **119**, e2200099119 (2022). https://doi.org/10.1073/pnas.2200099119

71 Malabarba, J. *et al.* ANNEXIN1 mediates calcium-dependent systemic defense in Arabidopsis plants upon herbivory and wounding. *New Phytol* **231**, 243-254 (2021). https://doi.org/10.1111/nph.17277

72 Kodavali, P. K. *et al.* Structural and functional characterization of annexin 1 from Medicago truncatula. *Plant Physiol Biochem* **73**, 56-62 (2013). https://doi.org/10.1016/j.plaphy.2013.08.010

73 Liao, C., Zheng, Y. & Guo, Y. MYB30 transcription factor regulates oxidative and heat stress responses through ANNEXIN-mediated cytosolic calcium signaling in Arabidopsis. *New Phytol* **216**, 163-177 (2017). https://doi.org/10.1111/nph.14679

74 Richards, S. L. *et al.* Annexin 1 regulates the H2O2-induced calcium signature in Arabidopsis thaliana roots. *Plant J* **77**, 136-145 (2014). https://doi.org/10.1111/tpj.12372

75 Laohavisit, A. *et al.* Arabidopsis annexin1 mediates the radical-activated plasma membrane Ca^{2}+- and K+-permeable conductance in root cells. *Plant Cell* **24**, 1522-1533 (2012). https://doi.org/10.1105/tpc.112.097881

76 Tichá, M. *et al.* Advanced Microscopy Reveals Complex Developmental and Subcellular Localization Patterns of ANNEXIN 1 in. *Front Plant Sci* **11**, 1153 (2020). https://doi.org/10.3389/fpls.2020.01153

77 Zhao, Z. X. *et al.* ANNEXIN 8 negatively regulates RPW8.1-mediated cell death and disease resistance in Arabidopsis. *J Integr Plant Biol* **63**, 378-392 (2021). https://doi.org/10.1111/jipb.13025

78 Vais, H. *et al.* ER-luminal [Ca. *Elife* **9** (2020). https://doi.org/10.7554/eLife.53531

79 Peiter, E. The plant vacuole: emitter and receiver of calcium signals. *Cell Calcium* **50**, 120-128 (2011). https://doi.org/10.1016/j.ceca.2011.02.002

80 Himschoot, E., Pleskot, R., Van Damme, D. & Vanneste, S. The ins and outs of Ca. *Curr Opin Plant Biol* **40**, 131-137 (2017). https://doi.org/10.1016/j.pbi.2017.09.003

81 Konopka-Postupolska, D. & Clark, G. Annexins as Overlooked Regulators of Membrane Trafficking in Plant Cells. *Int J Mol Sci* **18** (2017). https://doi.org/10.3390/ijms18040863

82 Carrasco-Castilla, J., Ortega-Ortega, Yolanda, Jáuregui-Zúñiga, David, Juárez-Verdayes, Marco A, Arthikala, Manoj-Kumar, Monroy-Morales, Elisabeth, Nava, Noreide, Santana, Olivia, Sánchez-López, Rosana, Quinto, Carmen. 108-119 (Environmental and Experimental Botany, 2018).

83 Liu, J. & Bisseling, T. Evolution of NIN and NIN-like Genes in Relation to Nodule Symbiosis. *Genes (Basel)* **11** (2020). https://doi.org/10.3390/genes11070777

84 Schnabel, E., Journet, E. P., de Carvalho-Niebel, F., Duc, G. & Frugoli, J. The Medicago truncatula SUNN gene encodes a CLV1-like leucine-rich repeat receptor kinase that regulates nodule number and root length. *Plant Mol Biol* **58**, 809-822 (2005). https://doi.org/10.1007/s11103-005-8102-y

85 Haseloff, J., Siemering, K. R., Prasher, D. C. & Hodge, S. Removal of a cryptic intron and subcellular localization of green fluorescent protein are required to mark transgenic Arabidopsis plants brightly. *Proc Natl Acad Sci U S A* **94**, 2122-2127 (1997). https://doi.org/10.1073/pnas.94.6.2122

86 Nelson, B. K., Cai, X. & Nebenführ, A. A multicolored set of in vivo organelle markers for co-localization studies in Arabidopsis and other plants. *Plant J* **51**, 1126-1136 (2007). https://doi.org/10.1111/j.1365-313X.2007.03212.x

87 Berg, S. *et al.* ilastik: interactive machine learning for (bio)image analysis. *Nat Methods* **16**, 1226-1232 (2019). https://doi.org/10.1038/s41592-019-0582-9

Acknowledgements

The *M. truncatula* R108 mutant plants utilized in this research project, which are jointly owned by the Centre National De La Recherche Scientifique, were obtained from Noble Research Institute, LLC and were created through research funded, in part, by grants from the National Science Foundation, NSF #DBI-0703285 and NSF #IOS-1127155. We thank S. Bensmihen for providing the *pEXT:DMI3* construct[51] and Celine Remblière for providing seeds of the *M. truncatula dmi3* line carrying the *pEXT:DMI3* construct. This work was supported by French National Research grants TULIP ANR-10-LABX-41, COME-IN ANR-14-CE35-0007-01 and LIVE-SWITCH ANR-19-CE20-0026-01 to FdCN and by the European Research Council (ERC) under the European Union's Horizon 2020 research and innovation program (grant No. 759731) to CG. A. G. was funded by an ANR postdoctoral grant (ANR-19-CE20-0026-01), A. K. and A. D. were funded by PhD grants from the French Ministry of National Education and Research. We acknowledge the TRI-FRAIB imaging facility, member of the national infrastructure France-BioImaging supported by the French National Research Agency (ANR-10-INBS-04).

Author contributions

Coordinated the work: FdCN; designed experiments: FdCN, AG, JF, AK, KH, MCA, LF, NFDF, CG; performed experiments: AG, JF, AK, KH, MCA, LF, AD, NFDF; Machine learning methods development: AG, ALR; phylogenetic analysis: JK, PMD; analysed data: AG, JF, AK, KH, MCA, LF, AD, LP, JK, PMD, CG, NFDF, FdCN; wrote the manuscript: FdCN, AG and JF.

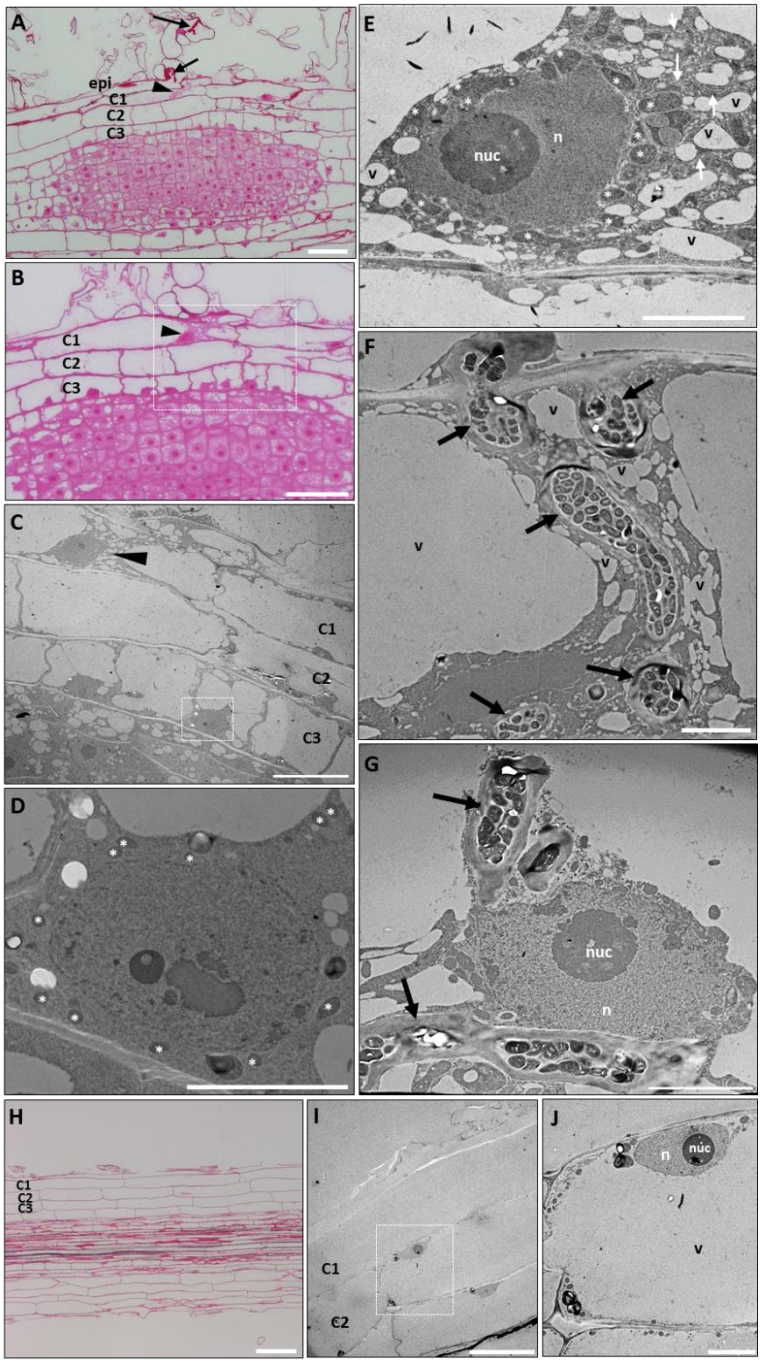

Fig. 1. Cell-specific structural changes in *M. truncatula* cells primed for infection.

(**A**-**B**) Representative images of longitudinal sections of *M. truncatula* A17 roots 5 days after spot-inoculation with *S. meliloti.* These are consecutive 1 µm sections stained with basic fuchsin to reveal cell outlines and content. Arrows indicate ITs in root hair epidermal cells and arrowheads indicate a C1 cortical cell exhibiting pre-infection priming. The region of interest in **B** (highlighted by a white square) is shown in **C**-**E** by transmission electron microscopy (TEM) of 80 nm sections. Note that the primed C1 outer cortical cell (arrowhead in **C**, and enlarged image in **E** exhibits a unique structural organization compared with neighbouring cells. Primed cells comprise a cytoplasmic bridge enriched in endoplasmic reticulum (white arrows in **E**), and numerous vesicles or small vacuole-like (SV-like) structures (SVs) (v). They also have a large nucleus (n) with enriched mitochondria (asterisks) around it, as quantified in Fig. S1. TEM

analysis of primed cells were performed in n=8 sections derived from 5 independent infection sites from 2 independent experiments. (**F**-**G**) At a later stage, when the IT (arrows) has progressed across the cytoplasmic bridge towards inner tissues, the nucleus of the crossed cell is frequently found closely associated to the IT (**G**). (**H**-**J**) Representative images of *M. truncatula* A17 root sections after mock (water) treatment for 5 days. (**H**) A 1 µm longitudinal section of a mock control root stained with basic fuchsin. (**I**-**J**) TEM of 80 nm sections of a mock control root. The region of interest in **I** (highlighted by a white square) is shown in **J**. Note that non-symbiotically activated cells have a large vacuole and nuclei near the cell periphery. Other abbreviations: cortical cells (C1, C2, C3), nucleolus (nuc). Scale bars: **A**-**B**, **H** = 50 µm, **C**, **I** = 20 µm, **D**-**G**, **J** = 5 µm. See additional primed cells and mitochondria quantification in Fig. S1.

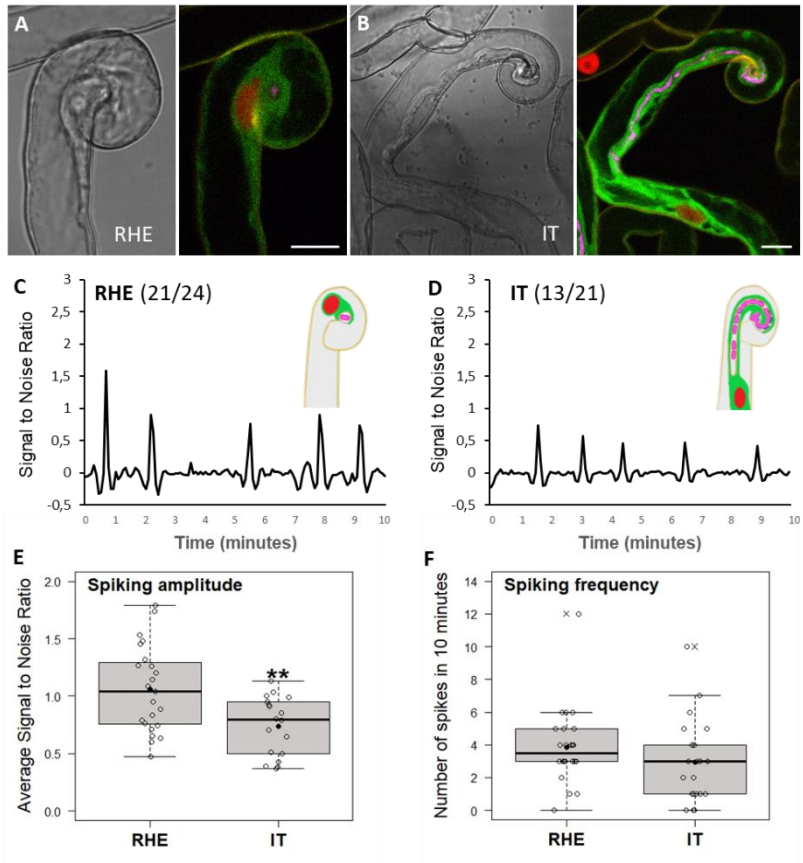

Fig. 2. Ca^{2+} spiking amplitude drops along root hair IT development.

(**A**-**B**) Representative bright-field and corresponding confocal images of (**A**) a root hair with entrapped CFP expressing (magenta)-*S. meliloti* (RHE) and (**B**) a root hair with a growing infection thread (IT) in *sunn*. Nuclei expressing the NR-GECO1 Ca^{2+} sensor appear in red, and the MtAnn1-GFP fluorescence (green) labels the cytoplasmic zone around the IT and the cytoplasmic bridge connecting and surrounding the nucleus. (**C**-**D**) Representative Ca^{2+} spiking traces of RHE (**C**) and growing IT stages (**D**) in *sunn*. The relative concentration of Ca^{2+} ions in the nucleus is reflected by the intensity of NR-GECO1 fluorescence, expressed as signal-to-noise ratio (SNR, cf. Methods section). The number of root hair with nuclear spiking/total number of root hairs are indicated between parentheses. Nuclei are counted as spiking when showing more than 2 peaks in 10 min. (**E**-**F**) Quantification of nuclear Ca^{2+} spiking: Spiking amplitude (**E**), expressed as average SNR of spikes per nucleus, and spiking frequency (**F**),

expressed as number of spikes in 10 minutes per nucleus. Box plots represent the distribution of individual values (indicated by open circles) from root hairs with entrapped rhizobia RHE, n=23 in **E** and n=24 in **F**) or with an IT (n=18 in **E** and n=21 in **F**) in *sunn,* 2-4 dpi with *S. meliloti* from three independent biological experiments. Median (central line), mean (solid black circle) and outliers (cross) are indicated. Two-tailed T-test (**E**) and Mann-Whitney test (**F**) of values were performed in R (asterisks indicate statistical difference; **p < 0.01). Scale bars: **A**-**B** = 10 µm. See also Fig. S2 and Movies 1-2 for Ca^{2+} spiking responses in A17 and/or *sunn* root hairs, and Figs. S4-S5 and S7 for MtAnn1-GFP localization and fluorescence quantification in root hair bridges.

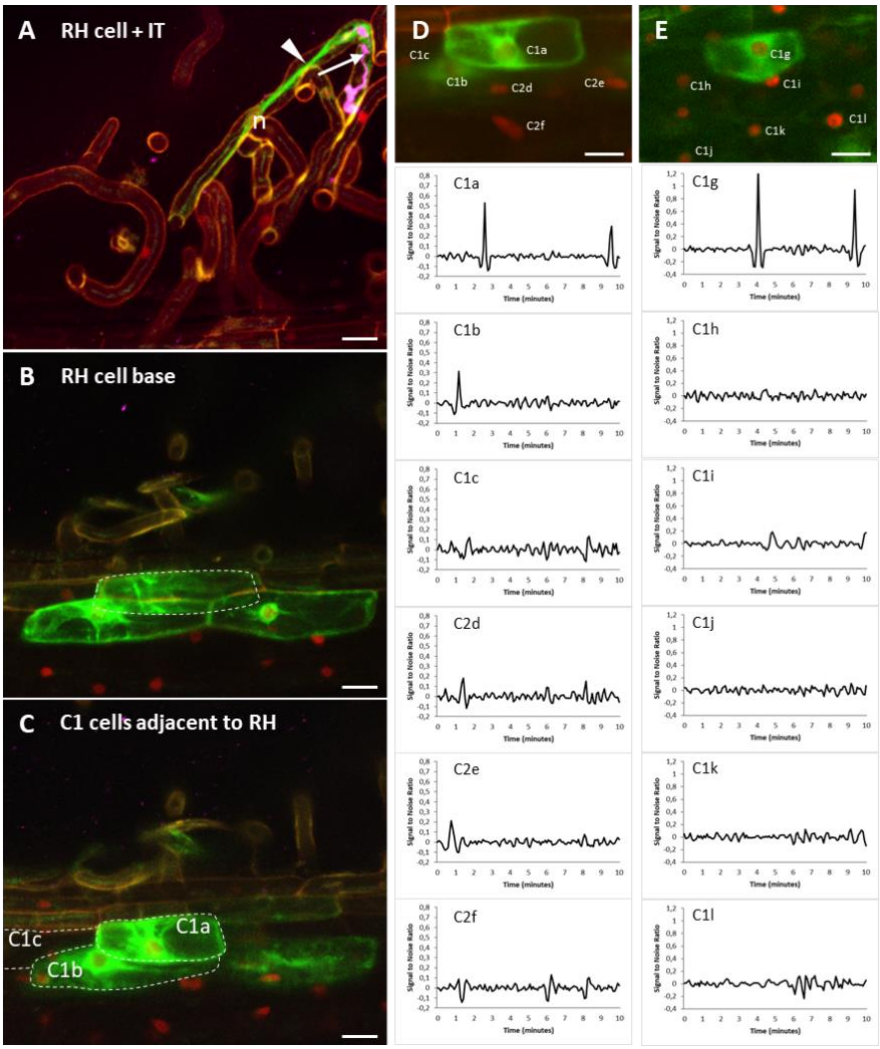

Fig. 3. Strong MtAnn1-GFP fusion fluorescence and low frequency Ca^{2+} spikes are hallmarks of pre-infection priming in the cortex.

Representative images of rhizobia infection sites in roots co-expressing MtAnn1-GFP (green) and NR-GECO1 (red) in *M. truncatula* A17. Confocal images from **A** to **C** illustrate an infected root hair with CFP-labelled rhizobia in IT (in magenta, arrow) and the nucleus (n) in front, guiding the growth of the IT in a cytoplasmic bridge (arrowhead) (**A**), the base of the root hair cell (**B**, dotted line) and the neighbour C1a-c outer cortical cells (**C**, dotted lines). C1a-C1c are also shown in **D**. (**D**-**E**) Representative traces of Ca^{2+} spiking from outer cortical cells from two

independent sites (C1a is also shown in **C**-**D**, and C1g in **E**, is from another site), adjacent to an infected root hair (shown in **A** for **D**, and not shown for the second site **E**). Traces from other neighbouring cortical cells (C1b-c, C2d-f in **D** and C1h-l in **E**) not in direct contact with the infection sites are shown. Cells are indicated in the upper panels. Images were obtained from A17 roots 4 dpi (**A**-**D**) or 3dpi (**E**) with *S. meliloti*. Note that only cortical cells co-expressing MtAnn1-GFP show detectable low frequency Ca^{2+} spiking (compare C1a-b and C1c, C1g and C1h-l, respectively). Traces are expressed as signal-to-noise ratio (SNR). Images in **A**-**C** are maximal z-projections of sub-stacks and images in **D**-**E** are maximal projections of whole time series. Scale bars: **A**-**E** = 20 µm. See also Figs. S3, S6 and S8 for Ca^{2+} spiking responses and MtAnn1-GFP dynamics in primed cells in the cortex in *sunn*. See also Fig. S3-S6 and Fig. S8-S9 and Movie 3.

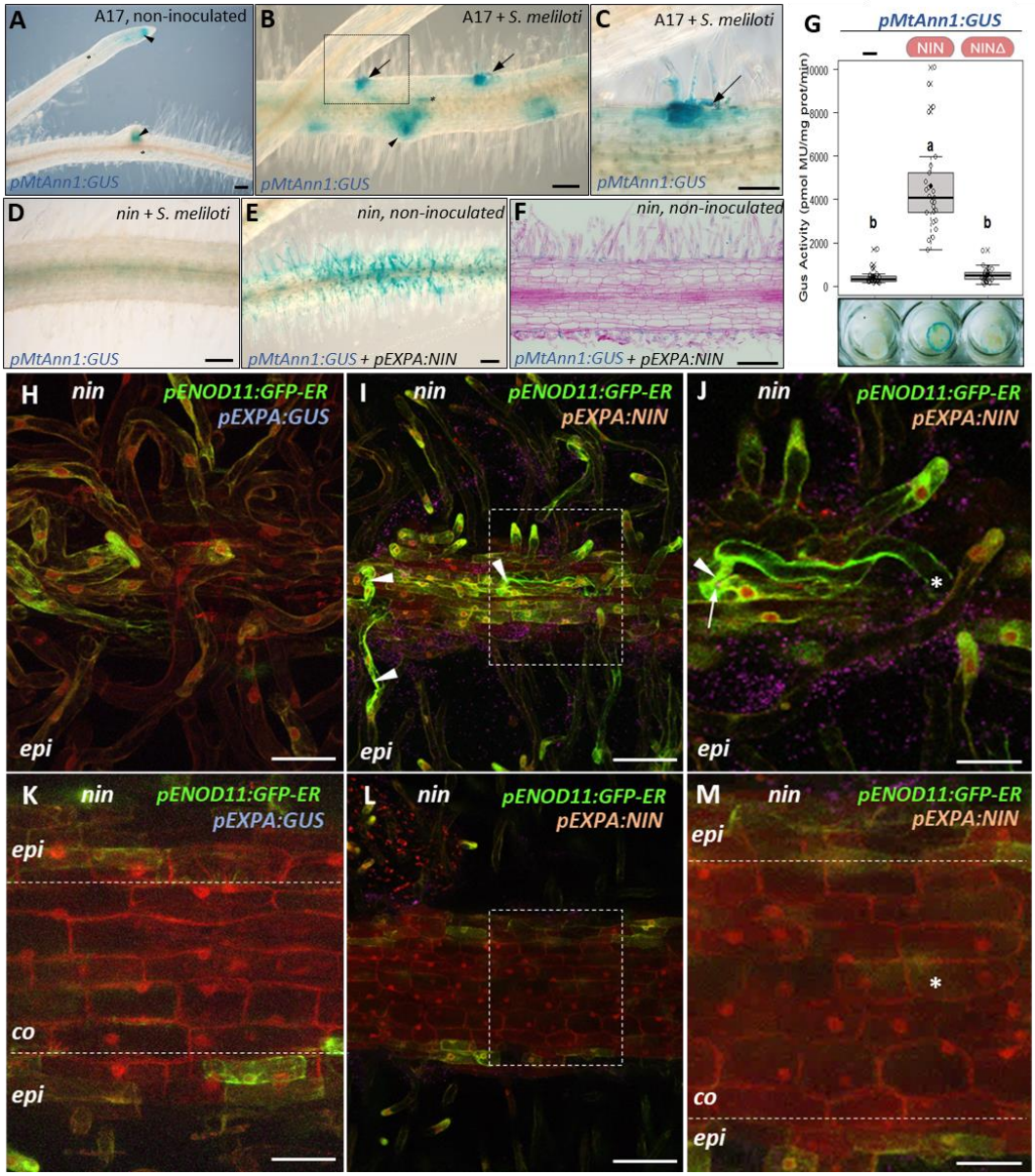

Fig. 4 NIN is required for cytoplasmic pre-infection priming and *MtAnn1* expression.

(**A**-**F**) Expression of the *pMtAnn1:GUS* fusion in *M. truncatula* A17 (**A**-**C**) or *nin* (**D**-**F**) roots non-inoculated (**A**, **E**-**F**) or inoculated with *S. meliloti* at 4 dpi (**B**-**D**). (**A**-**B**) *MtAnn1* exhibit constitute

promoter activity during root development (in root tips and developing lateral roots, arrowheads) and endodermal cells (asterisks). (**B**-**C**) Upon rhizobia inoculation, GUS activity is strongly detected at rhizobia infection sites (ITs, arrows in **B**-**C**). (**C**) A close view of an infection site (black square in **B**) enables to visualize *LacZ*-expressing rhizobia in magenta (arrow). (**D**-**F**) The infection-related expression profile of *MtAnn1* is abolished in rhizobia-inoculated *nin* roots (**D**). (**E**-**F**) Expression of NIN under the epidermis-specific promoter *pEXPA* in *nin* roots promotes *pMtAnn1:GUS* fusion activity in the epidermis, even in the absence of rhizobia (**E**-**F**). A longitudinal 10 µm root section counterstained with basic fushin show *pMtAnn1:GUS* activity (blue) restricted to the epidermal cell layer (**F**). Data in **A**-**F** are from two independent experiments (n=41 in A17, n=31 in *nin*, n=37 in *nin* + *pEXPA:NIN*). (**G**) Transactivation of the *pMtAnn1:GUS* fusion by NIN in *A. tumefaciens*-infiltrated leaf discs. Fluorimetric GUS assays were performed using 1 µg of total protein extracts. Box plots represent the distribution of values (indicated as open circles) of individual plants (n=25 per sample) from 4 independent experiments. Median (central line), mean (solid black circle) and outliers (cross) are indicated. Different letters above the box blots indicate statistically significant difference (One-way ANOVA, α= 5%). Images of representative leaf discs are included. (**H**-**M**) *pENOD11:*GFP-ER expression in *nin* transformed with *pEXPA:GUS* control (**H**, **K**) or complemented with *pEXPA:NIN* (**I**-**J**, **L**-**M**). Control or complemented *nin* roots all co-express the fluorescent marker *pUbiquitin*-DsRed, which labels cytosol and nucleoplasm in red. Green GFP-ER fluorescence labels the perinuclear ER network of epidermal cells and the tip of growing root hairs in **H**-**J**. (**I**-**J**)In complemented *nin*, GFP-ER also labels cytoplasmic columns (arrowheads) in rhizobia-enclosed (arrow in **J**) RHE stage root hairs. (**K**-**M**) In both control (**K**) and complemented *nin* roots (in **M**, boxed area in **L**), outer cortical cells (co) show no GFP-ER labelling. These Ds-Red labelled cells also show no signs of cytoplasmic reorganisation, whereas using the same Ds-Red marker we can detect cytoplasmic rearrangements in *sunn* (See Fig S11). **J** and **M** are higher magnification of boxed areas of **I** and **L**, respectively. Data were obtained from 2 independent experiments (n=7 for *nin* + *pEXPA:GUS* and n=19 for *nin* + *pEXPA:NIN*). Asterisks in **J** and **M** mark the xy positions of the infected root hair base. Abbreviations: epi=epidermis; co=cortex. Scale bars: **A**-**F** = 100 µm, **H**-**M** = 40 µm. See also Fig. S10-S11.

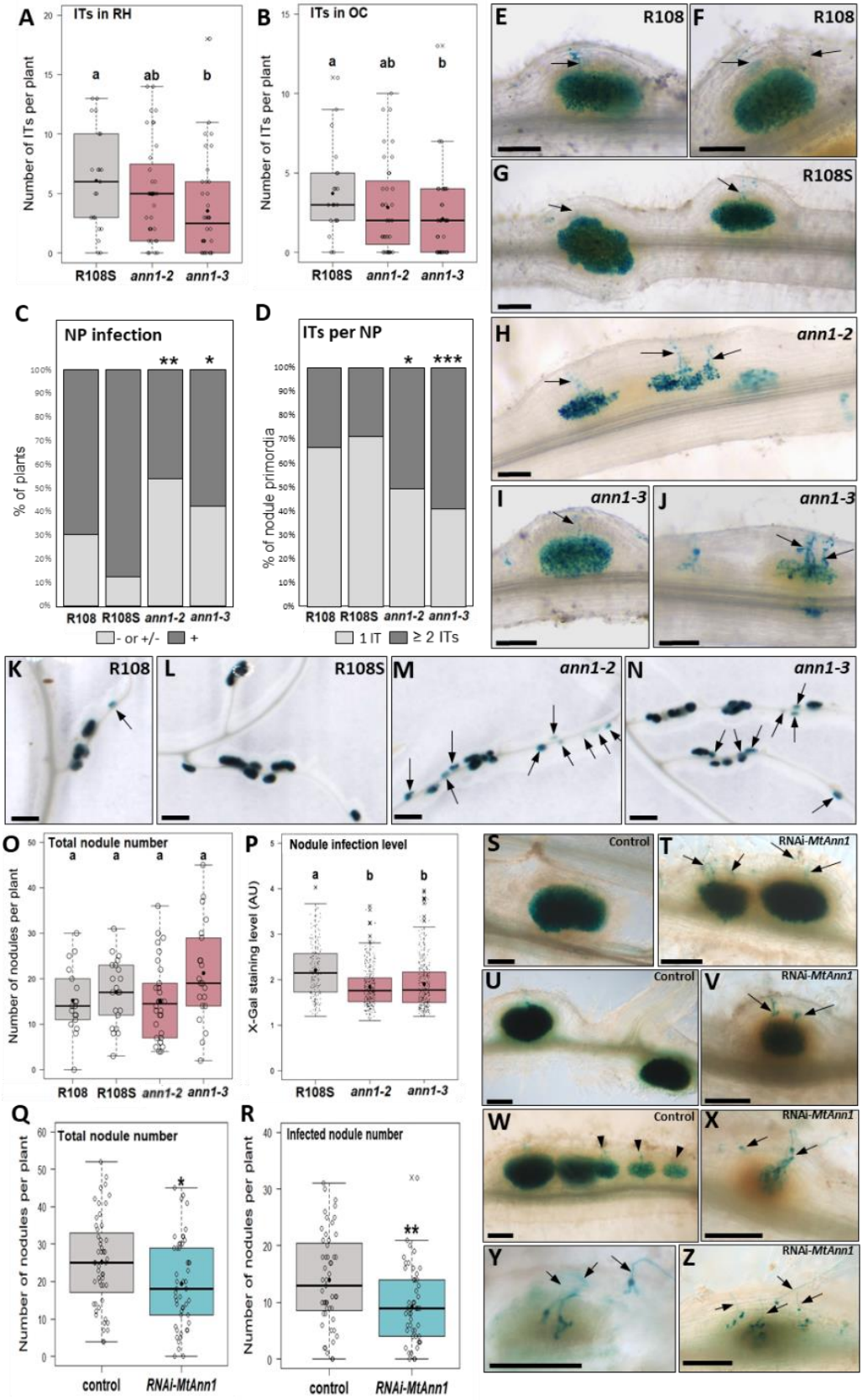

Fig. 5. Root Infection is negatively impacted in *ann1* mutants and RNAi transgenic roots.

Relative rhizobia infection levels were monitored in *ann1* mutants and *MtAnn1* RNAi transgenic roots with reduced *MtAnn1* or *MtAnn1/MtAnn2* expression levels (shown in Fig.

S12). Histochemical X-gal staining of mutant or RNAi *Medicago* roots (and corresponding controls) infected with a *lacZ*-expressing *S. meliloti* strain was used to quantify (**A**-**D**, **O**-**R**) and visualize (**E**-**N** and **S**-**Z**) rhizobia infection events in blue. (**A**-**J**) Early root infection by rhizobia was analyzed in root systems of R108 (n=17), R108S (n=21), *ann1-2* (n=36) and *ann1-3* (n=38) plants from 2 independent experiments at 4 dpi with rhizobia. The number of ITs in-root hairs (**A**) and ITs that had reached the outer cortex (**B**) are indicated. Different letters above the box blots indicate statistically significant difference (Kruskal-Wallis tests, α= 5%). (**C**-**D**) Graphs illustrate the proportion of plants having low to none (- or +/-) or colonized (+) nodule primordia (NP) (**C**), and of nodule primordia colonized by 1 or several ITs in *ann1* mutants compared to R108 and/or R108S lines (**D**). Asterisks in **C**-**D** indicate statistical differences relative to the R108S control (Fisher's exact tests, * $p < 0.05$, ** $p < 0.01$, *** $p < 0.001$). (**E**-**J**) Representative images of R108 (**E** and **F**), R108S (**G**), *ann1-2* (**H**) and *ann1-3* (**I** and **J**) infected nodule primordia at 4 dpi. (**K**-**N**) Representative images of R108, R108S and *ann1* nodules at 10 dpi with rhizobia. Note the higher proportions of less infected (arrows) nodules in mutants compared to WT lines. (**O**-**P**) R108, R108S, *ann1-2* and/or *ann1-3* nodule number (**O**) or infection levels (**P**) were analyzed 10 dpi with rhizobia. Infection levels (**P**) were quantified by automated ImageJ measurement of the intensity of bacterial X-gal blue staining of 10 dpi nodules on R108S (196 nodules from 21 plants), *ann1-2* (295 nodules from 30 plants) and *ann1-3* (310 nodules from 21 plants) roots, from 2 independent experiments. Different letters above the box blots indicate statistically significant differences (One-way ANOVA in 0 and Kruskal-Wallis in P tests, α = 5%). (**Q**-**Z**) RNAi knockdown of *MtAnn1* and *MtAnn2 in M. truncatula A17* roots. Total nodule/NP number (**Q**) and infected nodule/NP number (**R**) were quantified in in *M. truncatula* A17 roots expressing *pMtAnn1:GUS* (control) or *pMtAnn1:RNAi-MtAnn1* (*RNAi-MtAnn1*) at 5 dpi with *S. meliloti-LacZ* from 3 independent experiments (control, n=51 and *RNAi-MtAnn1,* n=50 plants). (**S**-**Z**) Representative images of nodules or NP formed in control (**S**, **U**, **W**) and *RNAi-MtAnn1* (**T**, **V**, **X**-**Z**). Fully colonized MtAnn1-RNAi nodules/NP with several ITs (arrows) are shown in **T**-**V**. Abnormal RNAi NPs are shown in **X**-**Z** compared to control NP (arrowheads in **W**). A two-tailed t-test (in **Q**) and a two-tailed Mann-Whitney test (in **R**) were performed in R (asterisks indicate statistical difference, * $p<0.05$, ** $p<0.01$). Box plots (**A**, **B**, **O**-**R**) represent the distribution of individual values (indicated as open circles in **A**-**B**, **O** and **Q**-**R,** and as black dots in **P**. Median (central line), mean (solid black circle) and outliers (crosses) are indicated. Scale bars: **E**-**J**, **S**-**Z** = 100 µm, **K**-**N** = 1mm**.** See also Fig. S12-S13.

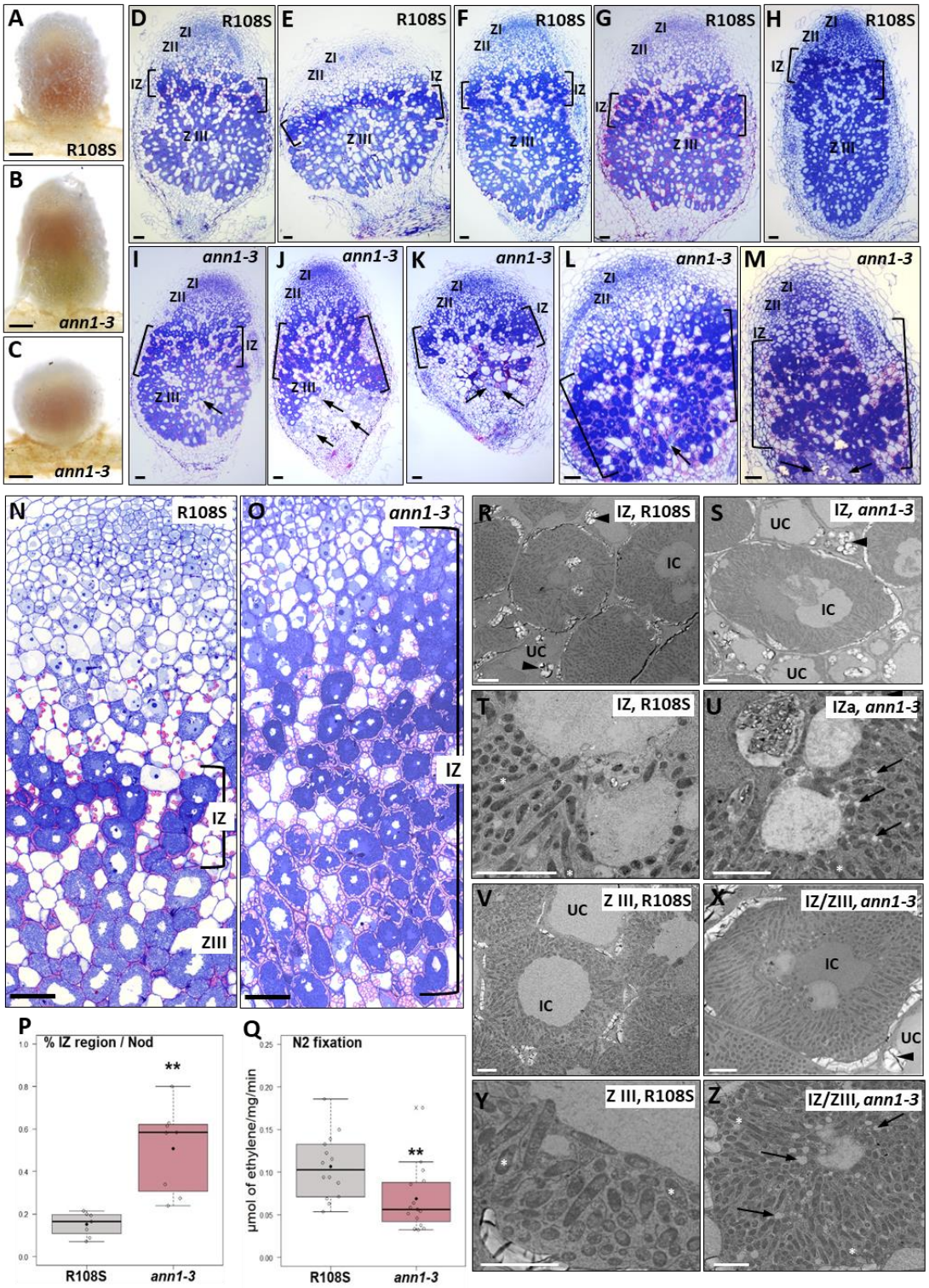

Fig. 6. *MtAnn1* mutants show impaired nodule differentiation and function.

(**A**-**C**) Representative images of entire nodules of wild-type R108S (**A**) and *ann1-3* mutants (**B**-**C**) collected at 15 dpi with *S. meliloti*. (**D**-**M**) Representative images of 1 µm longitudinal sections of 21 dpi nodules of R108S (**D**-**H** and **N**) and *ann1-3* (**I**-**M** and **O**) after staining with toluidine blue and/basic fuchsin. Meristematic (ZI), infection (ZII), interzone (IZ) and nitrogen fixing (ZIII) zones are labelled (**D**-**O**). The amyloplast-rich IZ is indicated between brackets in **D**-**O**. (**P**) Nodule IZ area was measured in images of 1 µm nodule sections from R108S (n=7) and *ann1-3* (n=8) and IZ relative proportion per nodule are shown for each genotype (see detailed

methodology in Fig. S14). (**Q**) Nitrogen fixation capacity was measured in nodulated root segments of R108S (n=14) and *ann1-3* (n=15) collected 21 dpi with *S. meliloti,* from 3 independent experiments (and comprising respectively 365 and 417 nodules). Box plots in **P**-**Q** represent the distribution of individual values (indicated as open circles). Median (central line), mean (solid black circle) and outliers (crosses) are indicated. Two-tailed Welsh (in **P**) or t-tests (in **Q**) of values were performed in R (asterisks indicate significant differences, **p<>0.01). (**R**-**Z**) Ultrastructural analyses by TEM of IZ or ZIII zones in R108S and *ann1-3* nodules. Close up of IZ (**R**-**U**) and IZ/ZIII (**V**-**Z**) of R108S or *ann1-3* nodules with uninvaded cells (UC) and invaded cells (IC) filled with bacteroids. Black arrowheads indicate amyloplasts located near intercellular spaces of IC and within UC cells in the IZ of R108S and *ann1-3,* and also in the IZ/ZIII of *ann1-3*. Differentiated bacteroids (white asterisks) are seen in both R108S and *ann1-3* (**T**, **U**, **Y** and **Z**). However, in *ann1-3* nodules they mostly appear as interzone-type bacteroids[55] imbedded in white vesicle-enriched region (black arrows). Scale bars: **A**-**C** = 1 mm, **D**-**O** = 50 µm, **R**-**Z** = 5 µm. See also Fig. S12-14 for complementary molecular and phenotypic description of *MtAnn1* mutants.

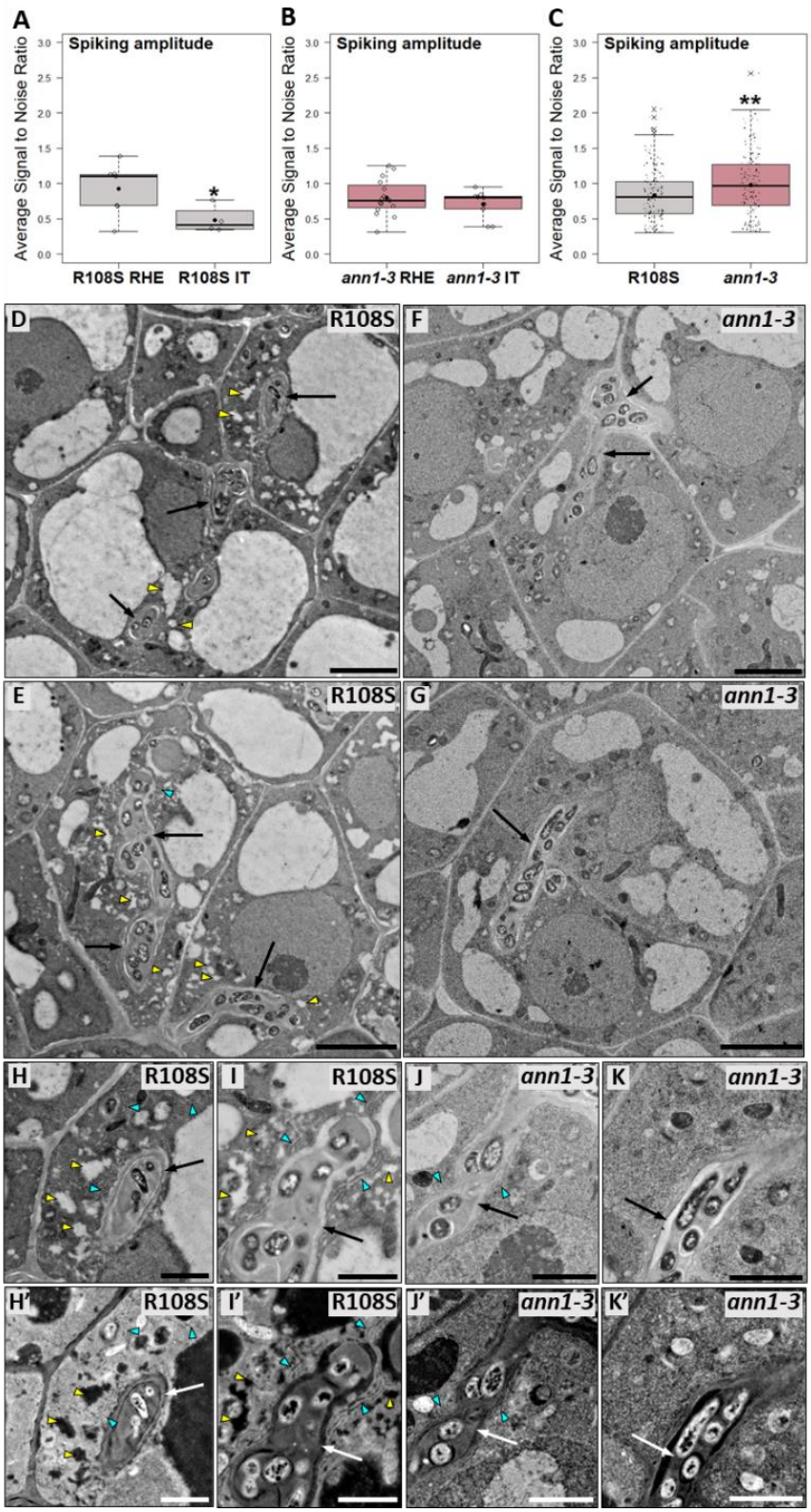

Fig. 7. Modified Ca^{2+} spiking and IT cytoplasmic environment in the absence of *MtAnn1*.

(**A**-**C**) Transgenic roots expressing the NR-GECO1 Ca^{2+} sensor were generated to monitor nuclear Ca^{2+} oscillations in in *ann1-3* mutant or wild-type (R108S) plants. Variations in Ca^{2+} ion concentration, through changes in the relative intensity of NR-GECO1 fluorescence, is expressed as signal-to-noise ratio (SNR, cf. Methods section). Box plots represent average amplitude of spikes (spike SNR), calculated separately for each nucleus of root hairs with

entrapped rhizobia (RHE) or with a growing IT (IT) in (**A**) R108S (R108S RHE, n=7; R108S IT, n=4) or in (**B**) *ann1-3* (*ann1-3* RHE, n=15; *ann1-3* IT, n=9) or in *S. meliloti*-responsive root hairs in the close competence zone (**C**) (R108S, n=160 and *ann1-3*, n=156) at 1-4 dpi. Data was obtained from three independent experiments. One-tailed t-tests (in **A**-**B**) and a two-tailed Mann-Whitney test (in **C**) were performed in R (asterisks indicate significant differences, *$p<0.05$; **$p<0.01$). Median (central line), mean (solid black circle) and outliers (cross) are indicated. (**D**-**K**) Transmission electron microscopy analyses of infected cells from apical zone 2 of WT R108S (**D**-**E**, **H**-**I**, and **H'-I'**) or *ann1-3* (**F**-**G**, **J**-**K**, and **J'**-**K'**) 15 dpi nodules. ITs (arrows) in WT are embedded in vesicles (yellow arrowheads) and ER-rich (blue arrowheads) cytoplasmic bridges, which are less visible in *ann1-3*. **H**'-**K**' are complementary inverted LUT images of **H**-**K** that were generated by ImageJ. Scale bars: **D**-**G** = 5 µm, **H**-**K** = 2 µm. See also Fig. S15.

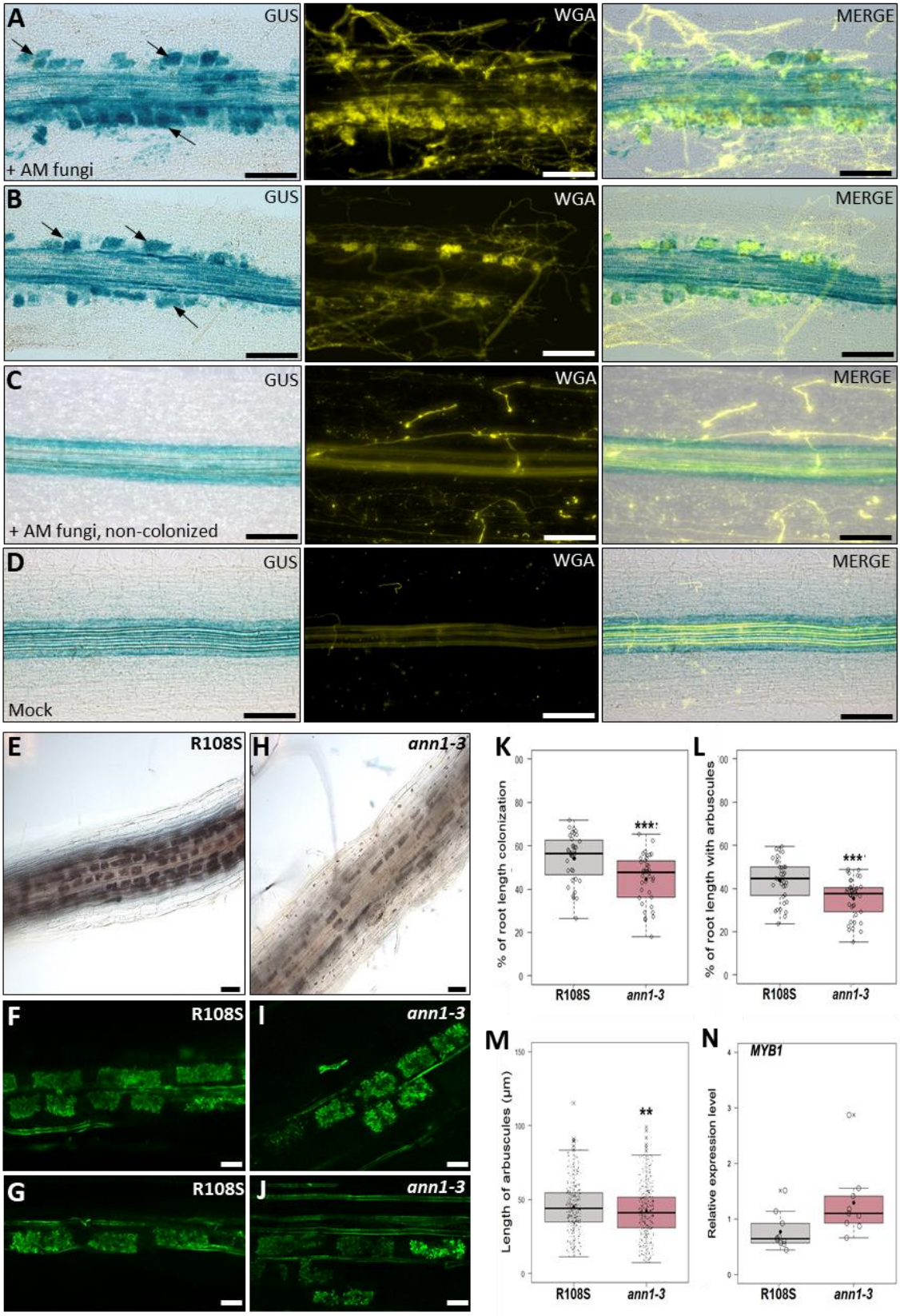

Fig. 8. *MtAnn1* is required for efficient mycorrhization *of M. truncatula* roots.

(**A**-**D**) *MtAnn1* promoter activity in independent *M. truncatula* roots after inoculation with *R. irregularis* at 4 wpi (**A**-**C**) or with water (mock) (**D**). Representative images of root sectors colonized (**A**-**B**) and non-colonized (**C**) by fungi are shown. Blue GUS staining in the root cortex

(arrows) correlates with *R. irregularis* colonized areas, visualized in yellow by WGA-Alexa Fluor 488 fluorescence staining (WGA). (**E**-**J**) Representative images of ink-stained AM-colonized roots (**E**-**H**) or WGA-stained arbuscules (**F**-**G**, **I**-**J**) formed in R108S or *ann1-3 M. truncatula* roots. (**K**-**L**) Determination of intraradical colonization by *R. irregularis* in WT and *ann1-3* plants by the gridline intersect method. The relative surface of the root system displaying vesicles, arbuscules and/or intraradical hyphae is given in (**K**), while the relative surface corresponding specifically to arbuscules is given in (**L**). Box plots represent values from R108S (WT) (n=36) and *ann1-3* (n=38) root systems at 6 weeks post-inoculation (wpi), from two independent biological experiments. (**M**) Relative arbuscule lengths were compared in R108S (WT) and *ann1-3* roots. (**N**) Q-RT-PCR expression analysis of *MYB1* in total RNA samples from independent R108S (WT) (n=10) or *ann1-3* (=9) plants inoculated with *R. irregularis* (6 wpi, 2 independent experiments). Individual values (open circles or black dots), median (central line) and mean (solid black circle) are indicated in **K**-**N**. Two-tailed Student (**K**-**L**, **N**) and Mann Whitney (**M**) tests were performed in R (asterisks indicate significant differences, **$p<0.01$, ***$p<0.001$). Scale bars: **A**-**D** = 100 µm, **E**-**H** = 50 µm, **F**-**J** = 20 µm. See also Fig. S16.